Article

Cell

Snake Venom Gland Organoids

Graphical Abstract

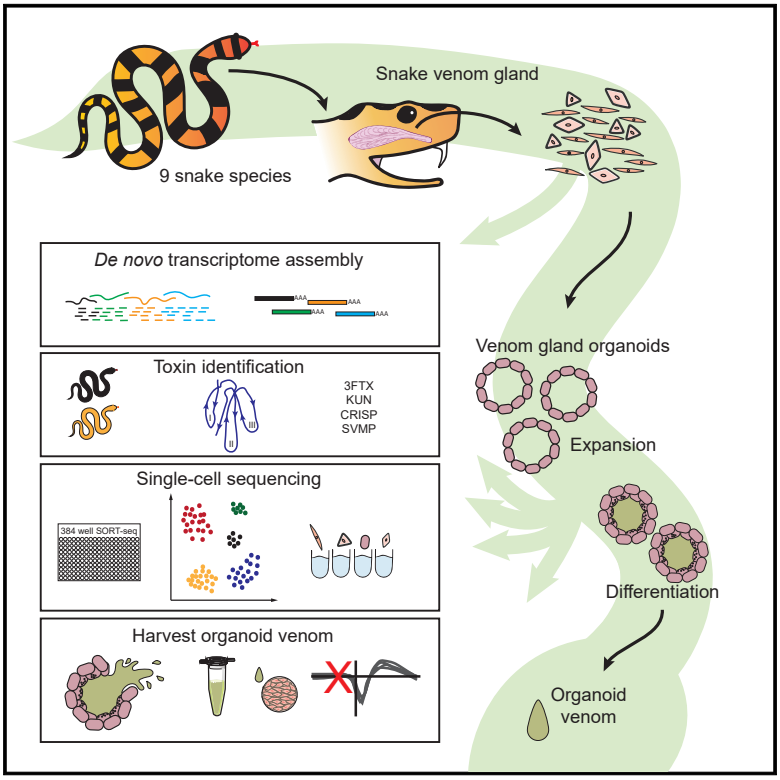

Authors

Yorick Post, Jens Puschhof, Joep Beumer, ..., Michael K. Richardson, Nicholas R. Casewell, Hans Clevers

Correspondence

h.clevers@hubrecht.eu

In Brief

The establishment of venom gland organoids from a variety of snake species allows for the production and harvest of different types of toxins of biological interest.

Highlights

- Snake venom gland cells can be cultured as adult-stem-cell-based organoids
- Organoids contain proliferating progenitors and various venom-producing cells
- Regional and cellular heterogeneity of venom components is maintained in culture
- Venom gland organoids secrete functionally active toxins

Post et al., 2020, Cell *180*, 233–247
January 23, 2020
https://doi.org/10.1016/j.cell.2019.11.038

CellPress

Cell

Snake Venom Gland Organoids

Yorick Post,[1,2,16] Jens Puschhof,[1,2,16] Joep Beumer,[1,2,16] Harald M. Kerkkamp,[3,4] Merijn A.G. de Bakker,[4] Julien Slagboom,[5] Buys de Barbanson,[1,2] Nienke R. Wevers,[6,7] Xandor M. Spijkers,[6,8] Thomas Olivier,[6] Taline D. Kazandjian,[9] Stuart Ainsworth,[9] Carmen Lopez Iglesias,[10] Willine J. van de Wetering,[1,10] Maria C. Heinz,[2,11] Ravian L. van Ineveld,[2,12] Regina G.D.M. van Kleef,[13] Harry Begthel,[1,2] Jeroen Korving,[1,2] Yotam E. Bar-Ephraim,[1,2] Walter Getreuer,[14] Anne C. Rios,[2,12] Remco H.S. Westerink,[13] Hugo J.G. Snippert,[2,11] Alexander van Oudenaarden,[1,2] Peter J. Peters,[10] Freek J. Vonk,[3] Jeroen Kool,[5,15] Michael K. Richardson,[4] Nicholas R. Casewell,[9] and Hans Clevers[1,2,12,17,*]

[1]Hubrecht Institute, Royal Netherlands Academy of Arts and Sciences (KNAW) and UMC Utrecht, 3584 CT Utrecht, the Netherlands
[2]Oncode Institute, Hubrecht Institute, 3584 CT Utrecht, the Netherlands
[3]Naturalis Biodiversity Center, 2333 CR Leiden, the Netherlands
[4]Institute of Biology Leiden, Department of Animal Science and Health, 2333 BE Leiden, the Netherlands
[5]Division of BioAnalytical Chemistry, Department of Chemistry and Pharmaceutical Sciences, Vrije Universiteit Amsterdam, 1081 LA Amsterdam, the Netherlands
[6]Mimetas BV, Organ-on-a-Chip Company, 2333 CH Leiden, the Netherlands
[7]Department of Cell and Chemical Biology, Leiden University Medical Centre, Einthovenweg 20, 2333 ZC Leiden, the Netherlands
[8]Department of Translational Neuroscience, Utrecht University Medical Center, 3584 CG Utrecht, the Netherlands
[9]Centre for Snakebite Research & Interventions, Department of Tropical Disease Biology, Liverpool School of Tropical Medicine, Liverpool L3 5QA, UK
[10]The Maastricht Multimodal Molecular Imaging Institute, Maastricht University, 6229 ER Maastricht, the Netherlands
[11]Molecular Cancer Research, Center for Molecular Medicine, University Medical Center Utrecht, Utrecht University, 3584 CX Utrecht, the Netherlands
[12]The Princess Maxima Center for Pediatric Oncology, 3584 CS Utrecht, the Netherlands
[13]Neurotoxicology Research Group, Division of Toxicology, Institute for Risk Assessment Sciences (IRAS), Utrecht University, 3584 CL Utrecht, the Netherlands
[14]Serpo, 2288 ED Rijswijk, the Netherlands
[15]Division of BioAnalytical Chemistry, Department of Chemistry and Pharmaceutical Sciences, Amsterdam Institute for Molecules Medicines and Systems, Vrije Universiteit Amsterdam, 1081 HV Amsterdam, the Netherlands
[16]These authors contributed equally
[17]Lead Contact
*Correspondence: h.clevers@hubrecht.eu
https://doi.org/10.1016/j.cell.2019.11.038

SUMMARY

Wnt dependency and Lgr5 expression define multiple mammalian epithelial stem cell types. Under defined growth factor conditions, such adult stem cells (ASCs) grow as 3D organoids that recapitulate essential features of the pertinent epithelium. Here, we establish long-term expanding venom gland organoids from several snake species. The newly assembled transcriptome of the Cape coral snake reveals that organoids express high levels of toxin transcripts. Single-cell RNA sequencing of both organoids and primary tissue identifies distinct venom-expressing cell types as well as proliferative cells expressing homologs of known mammalian stem cell markers. A hard-wired regional heterogeneity in the expression of individual venom components is maintained in organoid cultures. Harvested venom peptides reflect crude venom composition and display biological activity. This study extends organoid technology to reptilian tissues and describes an experimentally tractable model system representing the snake venom gland.

INTRODUCTION

Snakebite envenoming is a neglected tropical disease estimated to be responsible for >100,000 deaths worldwide each year (Gutiérrez et al., 2017). Upon injection through specialized fangs, venomous snakes primarily use their venom to immobilize prey. For numerous snake species, the venom delivered by a single bite is enough to kill prey that is many times larger than the snake. During vertebrate evolution, the snake venom gland has been adapted from the salivary gland (Kochva, 1987). Secretory columnar cells in the gland epithelium secrete a complex mixture of peptides and proteins, stored in the lumen and channeled to the fangs through connecting ducts. Venom toxins are classified into distinct protein families with diverse modes-of-action (Fry et al., 2009), which makes them a rich source for drugs targeting human proteins (Clark et al., 2019). Snake venoms differ greatly in toxin composition and the architecture of the machinery involved in its production and release. Venom from viperid snakes (such as the rattlesnake) mainly consists of hemotoxic enzymes (Ainsworth et al., 2018), whereas elapids (such as the king cobra) typically produce smaller peptides with neurotoxic effects (Vonk et al., 2013). Three-finger toxins (3FTxs) constitute a diverse and highly expressed class of toxins that mainly exert a neurotoxic effect through interaction with acetylcholine

receptors (Tsetlin, 2015). Kunitz-type protease inhibitors (KUNs) also exert neurotoxic activities, although some are anticoagulant (Harvey, 2001; Millers et al., 2009). Phospholipase A2 (PLA2) proteins can act as myotoxins or neurotoxins and display anti-platelet activities (Gutierrez and Lomonte, 2013), whereas cysteine-rich secretory proteins (CRISPs) block smooth muscle contraction (Yamazaki and Morita, 2004). Finally, snake venom metalloproteinases (SVMPs), L-amino acid oxidases (LAAOs), and C-type lectins (CTLs) mostly disrupt blood coagulation (Slagboom et al., 2017; Izidoro et al., 2014). Much still needs to be learned about toxin production and release cycles, heterogeneity of venom-producing cells, and factors influencing venom composition.

Organoids are defined as self-organizing 3D structures that can be grown from stem cells and that recapitulate essential features of the tissue under study (Clevers, 2016). We originally showed that a serum-free medium containing R-spondin, epidermal growth factor (EGF), and Noggin suffices to support the growth of mouse Lgr5$^+$ intestinal ASCs into ever-expanding epithelial organoids. These "mini-guts" contain all known cell types of the gut lining (Sato et al., 2009), observations that were extended through single-cell RNA sequencing (Grün et al., 2015; Beumer et al., 2018; Gehart et al., 2019). Subsequently, similar R-spondin-based protocols have been reported for a wide diversity of healthy and diseased mammalian epithelia (Artegiani and Clevers, 2018). Of interest to the current study, Maimets et al. (2016) have demonstrated the feasibility of growing mammalian salivary gland organoids.

Little is known about the biology of adult stem cells in reptiles. Different short-term culture systems have been described for snake venom glands (Sells et al., 1989; Carneiro et al., 2006), yet long-term cultures capturing structural and functional properties of the snake venom gland have not been developed. Here, we aim to establish long-term culture conditions for functional snake venom gland epithelium using R-spondin-based organoid technology.

RESULTS

Epithelial Organoid Cultures Derived from Snake Venom Glands

Venom glands from nine different snake species, representing members of both the Elapidae (*Naja pallida*, *Naja annulifera*, *Naja nivea*, *Naja atra*, and *Aspidelaps lubricus cowlesi*) and Viperidae (*Echis ocellatus*, *Deinagkistrodon acutus*, *Crotalus atrox*, and *Bitis arietans*) families, were dissociated and embedded in basement membrane extract (BME) at 32°C (Figure 1A). Supplying a medium containing a "generic" mammalian organoid cocktail (see below) resulted in initial expansion of organoids for all species (Figures 1B and S1A) (some were subsequently lost due to bacterial contamination, insensitive to the antibiotics used). Passaging yielded expanding organoids that histologically resembled the original gland epithelium (Figure 1C). The venom gland organoids could be expanded optimally using R-spondin (the Wnt signal-amplifying ligand of Lgr5) (de Lau et al., 2011), the BMP inhibitor Noggin, EGF, the small molecule TGF beta inhibitor A83-01, PGE2, and FGF10 (Figures 1D and S1B). This "expansion medium" controls the same cellular signaling pathways that are required for mammalian epithelial organoids (Fatehullah et al., 2016). Reptilian organoid expansion was only successful at lower temperatures (Figure S1C), consistent with the average body temperature of poikilotherm species such as snakes. When cultured at 37°C, the standard for mammalian cells, a heat shock response (*HSPA8*) was observed within 2 h, which is described to preclude cell division, and consequently prohibited organoid growth (Richter et al., 2010) (Figure S1D). The proliferating cells self-organized into cystic spheres lined by a simple polarized epithelium (Figure 1E; Video S1), while budding of organoids was occasionally observed. Under these conditions, organoids expanded exponentially for >20 passages without significant changes in growth kinetics or morphology (Figure 1B). As demonstrated previously for mammalian organoids (Bolhaqueiro et al., 2018), a lentiviral construct encoding histone 2B coupled to a fluorescent protein (H2B-RFP) allowed visualization of the organoid chromatin (Figure S1E).

Newly Assembled Transcriptome Reveals High Toxin Expression in Organoids

Simultaneous withdrawal of all growth factors (with the exception of PGE2 to maintain cystic organoids) for 7 days resulted in less-proliferative organoids (Figure 2A). These organoids contained highly polarized cells with secretory vesicles, described previously as the main producers of venom in the snake venom gland (Mackessy, 1991) (Figure 2B). Furthermore, ciliated cells could occasionally be observed by electron microscopy (Figure S1F). High-speed imaging captured functionally beating cilia in a subset of organoids (Video S2). Based on these features of apparently mature and functional cell types, we defined this cultured condition as our "differentiation" cocktail.

Snake venom contains dozens to hundreds of different bioactive compounds (Fox and Serrano, 2008). No annotated genome exists for *A. l. cowlesi.* To gain deeper insight into the expression of individual toxin-encoding genes, we assembled a *de novo* transcriptome of *A. l. cowlesi* using Trinity (Haas et al., 2013) (Figure 2C). Libraries of contigs (311,948) generated from late-embryonic liver, pancreas, and venom gland as well as from venom gland organoids were used to determine gene-expression levels for each of the three tissues as well as the venom gland organoids. The organoid transcriptome showed toxins to represent the dominant class of expressed genes, while homologs of established markers of mammalian liver and pancreas were restricted to their corresponding organ (Figure 2D). Toxin expression in venom gland tissue was markedly lower compared to organoids, most likely due to presence of non-epithelial cells in gland tissue. Among the toxins, 3FTxs were most abundant (Figure 2E). We also detected expression of CRISPs, SVMPs, and KUNs (Figures 2E and S1G). The relative abundance of these toxin classes matched the venom gland tissue at transcriptome level and the crude venom composition at protein level (Whiteley et al., 2019) (Figure 2E). Of note, the 7-day differentiation protocol increased overall toxin gene expression but reduced the expression of CRISP (Figures 2D and 2E). We concluded that *A. l. cowlesi* organoids produced a near-normal spectrum of venom factors.

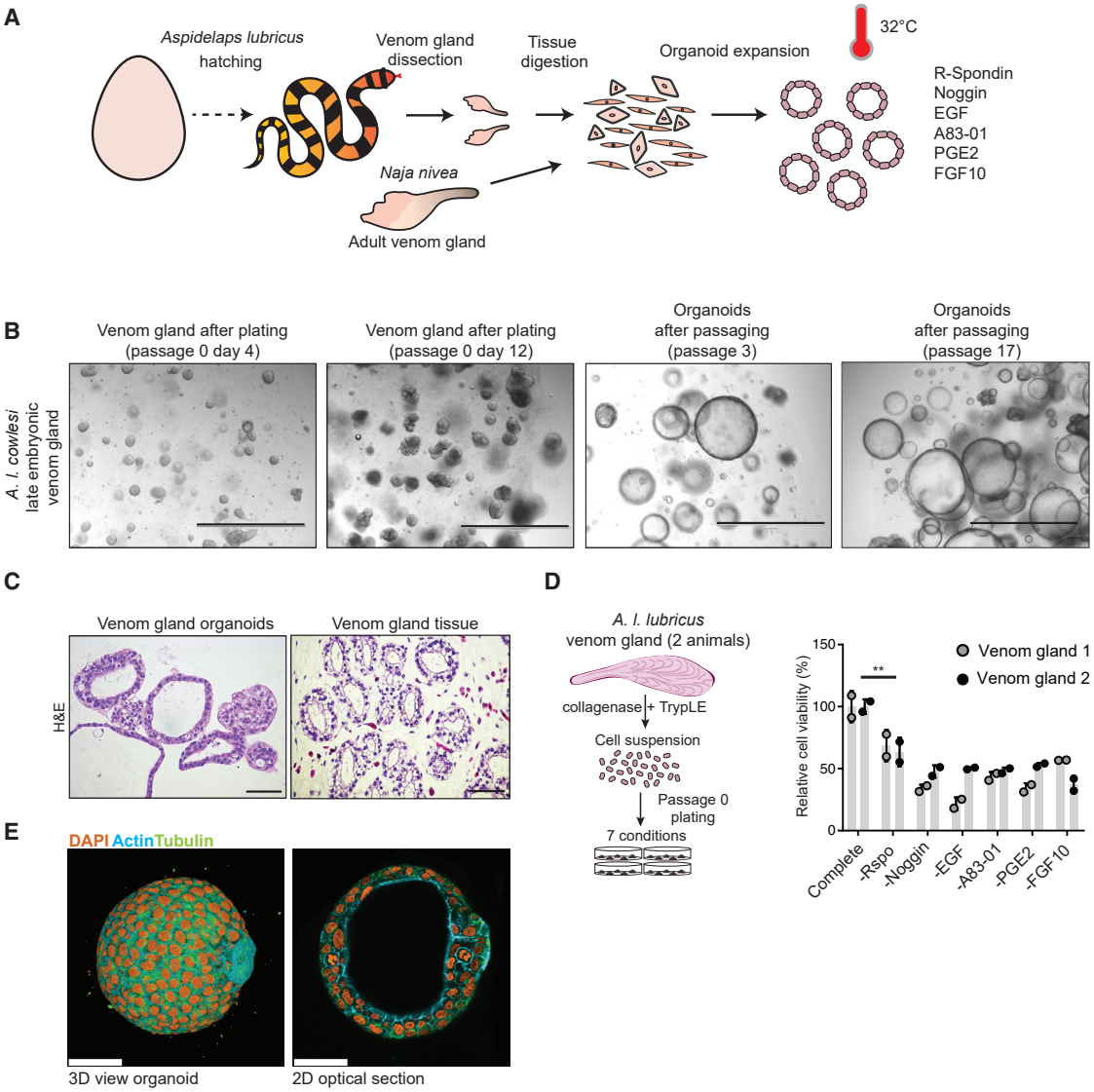

Figure 1. Establishment of Organoid Culture Conditions for Snake Venom Gland

(A) Schematic representation of the derivation of venom gland organoids from late embryonic (~7–2 days before hatching) *A. l. cowlesi* (n = 7) (see also Figure S1A).

(B) Time course of organoid expansion after seeding of cells from a single *A. l. cowlesi* venom gland in BME (passage 0) until passage 17. Scale bars, 1,000 μm.

(C) Haematoxylin and eosin (H&E) stain of late embryonic *A. l. cowlesi* venom gland and organoids. Scale bars, 50 μm.

(D) Schematic representation of medium component dropout screen on primary tissue outgrowth. Quantification of relative cell viability per condition after 14 days, normalized to complete expansion medium (see also Figure S1B). Data points represent biological replicates. ** = $p \leq 0.01$.

(E) Immunofluorescent staining of organoid for DNA (DAPI), tubulin (green), and actin (blue). Scale bars, 50 μm.

See also Figure S1.

Adult *Naja nivea* Venom-Gland-Derived Organoids

To further demonstrate the long-term propagation capacity of adult venom-gland-derived cells using our protocol, we expanded organoids from *Naja nivea*, the Cape cobra. Venom glands from a euthanized adult individual (>1-year-old) were dissociated and cultured using the same conditions as used above (Figure 3A). Organoids recapitulated the epithelial phenotype and were expanded for over 18 passages (Figures 3A and 3B). While cells were viable and proliferating in "expansion medium," we noticed reduced swelling (smaller lumen) in *N. nivea* organoids making it more difficult to mechanically split these cultures. Upon additional activation of cyclic AMP using forskolin (FSK), organoids exhibited improved swelling allowing easier splitting (Figure 3C). For further passaging (after passage 5) of *N. nivea* organoids, we supplemented expansion medium with FSK. Forskolin-induced swelling is well known in primary human intestinal organoids, where it is used to monitor the ability to transport chloride ions (Dekkers et al., 2013).

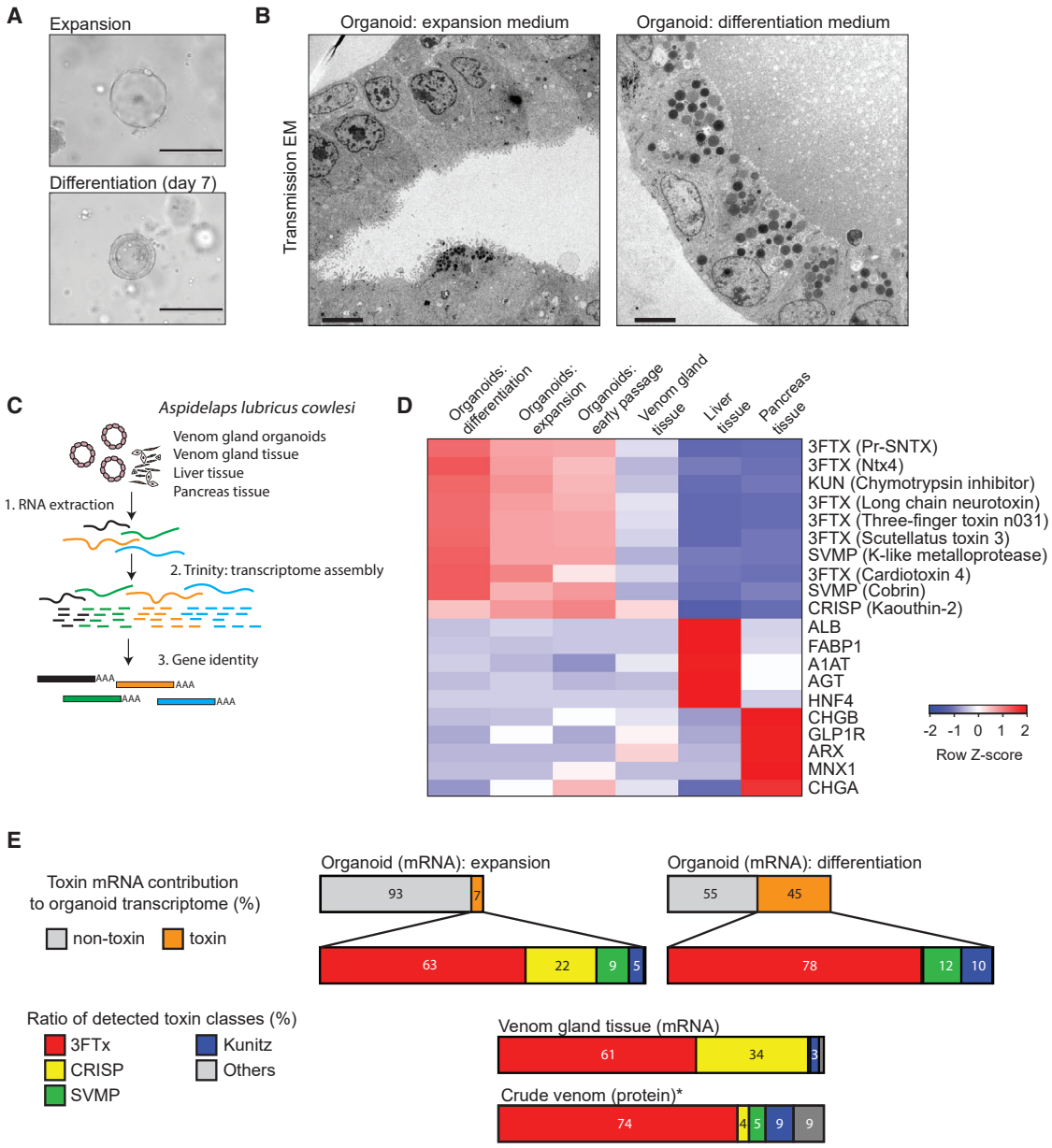

Figure 2. Venom Gland Organoids Express a Near-Normal Spectrum of Toxins

(A) Representative bright-field images of organoids after seven days expansion medium or differentiation medium. Scale bars, 200 μm.

(B) Transmission electron microscopy (TEM) of organoids in expansion and differentiation medium shows simple epithelial cells and polarized exocrine cells with secretory vesicles oriented toward the lumen. Scale bars, 5 μm.

(C) Schematic representation of *de novo* transcriptome assembly using Trinity. Input contained late embryonic *A. l. cowlesi* RNA isolated from venom gland tissue, pancreas tissue, liver tissue, and three venom gland organoid samples (early passage expansion, late passage expansion, late passage differentiation).

(D) Heatmap of organoid and tissue gene expression determined by mRNA sequencing mapped on *de novo* transcriptome. Highlighted are highly expressed toxin classes (*3FTX*, *KUN*, *SVMP*, *CRISP*), as well as liver and pancreas markers.

(E) Contribution of toxin-encoding genes (orange) and non-toxin genes (gray) to the transcriptome per sample, and the contribution of toxin classes in expansion medium and differentiation medium compared to venom gland tissue mRNA and venom proteome. *Dataset from Whiteley et al., 2019.

3FTx, three-finger toxin; CRISP, cysteine-rich secretory protein; SVMP, snake venom metalloproteinase; Kunitz, Kunitz trypsin inhibitor; others include cobra venom factor (CVF), L-amino acid oxidase (LAOO), and phosphodiesterases (PDE).

See also Figure S1G.

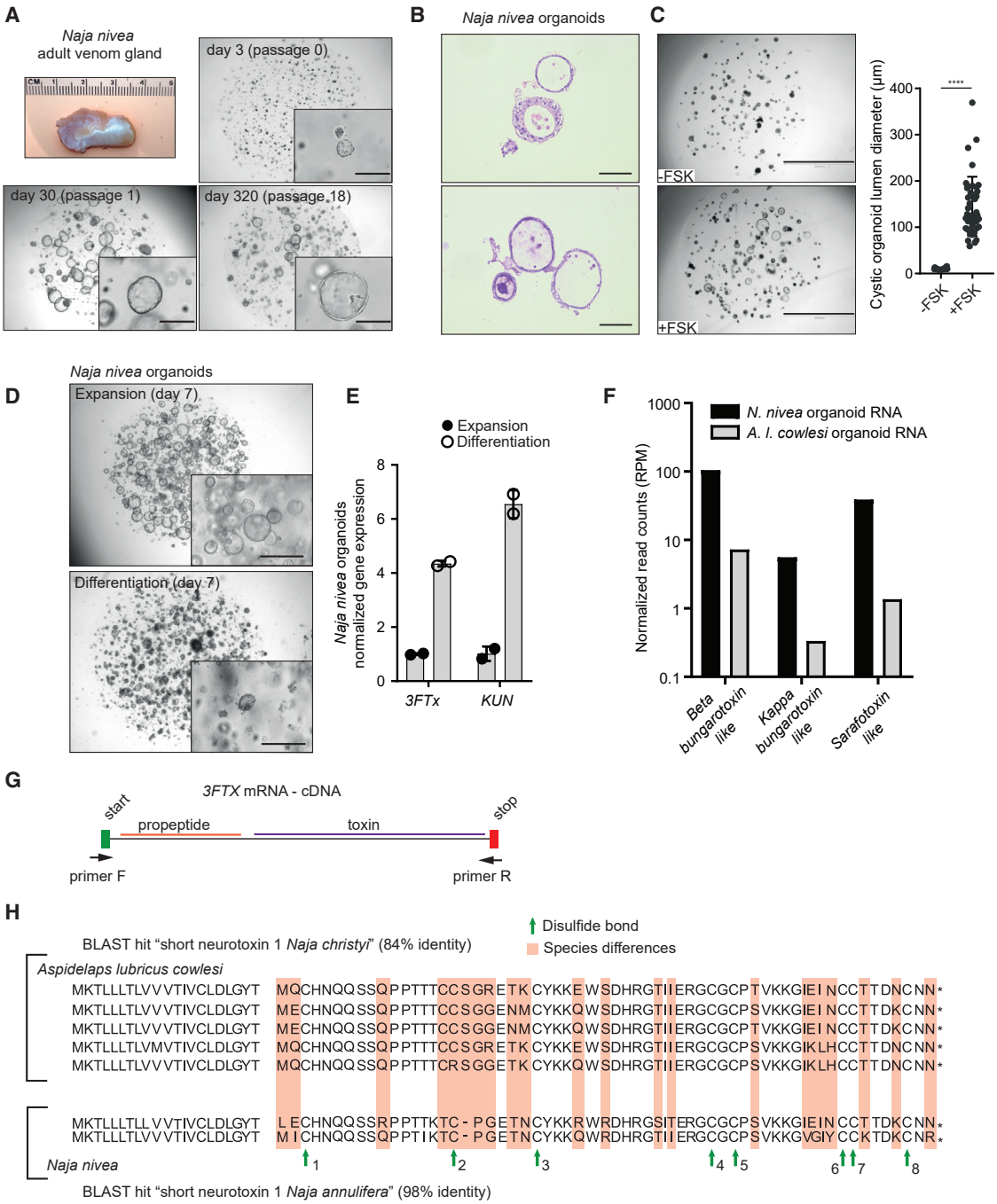

Figure 3. *Naja nivea* Organoids Derived from Adult Venom Gland Reveal Species-Specific Toxins

(A) Adult *Naja nivea* venom gland (n = 2) and organoid outgrowth after seeding of primary cells (passage 0) until passage 18 (related to Figure S1A). Scale bars, 200 µm.

(B) H&E and PAS staining of *Naja nivea* organoids derived from an adult venom gland. Scale bars, 50 µm.

(C) Bright field images and quantification of *Naja nivea* organoids grown in complete expansion medium with or without supplementation of forskolin (FSK) and matching quantification. Data points represent individual organoids. Scale bars, 2,000 um. **** = $p \leq 0.0001$.

(D) Bright field images of *Naja nivea* organoids after 7 day expansion or differentiation protocol. Scale bars, 200 µm.

(E) Gene expression of toxins (*3FTX* and *KUN*) in *N. nivea* organoids upon exposure to expansion or differentiation medium (7 days). Determined by qPCR, normalized to *ACTB* and relative to expansion medium. Data points represent biological replicates.

(legend continued on next page)

Exposure to "differentiation medium," including the withdrawal of FSK resulted in the expected phenotype of less proliferative organoids (Figure 3D) accompanied by increased expression of *3FTx* and *KUN* by qPCR (Figure 3E). To establish a "deep" gene expression profile, we performed bulk mRNA sequencing of *N. nivea* organoids in differentiation medium. PolyA enriched reads could be mapped to the *de novo A. l. cowlesi* transcriptome (Figure 2C). We thus identified a number of putative toxins enriched in organoids from *N. nivea*, such as beta-bungarotoxin-like, kappa-bungarotoxin-like, and sarafotoxin-like (Figure 3F). 3FTxs are the main venom components of elapid snakes. Utilizing the high sequence conservation of *3FTX*, we were able to PCR-amplify the coding sequence of several variants starting from *A. l. cowlesi* and *N. nivea* organoid cDNA (Figure 3G). When translating these *3FTX* coding sequences *in silico*, we detected peptide sequences that have not been described before in the NCBI database and are specific to the individual species (Figure 3H).

Because our access to *A. l. cowlesi* venom gland material was more regular (one clutch a year), we focused our further characterization on organoid lines derived from *A. l. cowlesi*.

Organoids Display Cellular Heterogeneity in Toxin Expression

The cellular heterogeneity of the venom gland epithelium has largely been described morphologically. We have recently demonstrated the usefulness of organoids for the detailed delineation of cell lineages in the enteroendocrine compartment of the gut (Beumer et al., 2018). Using a similar strategy, we performed single-cell RNA sequencing of organoids in expansion and differentiation medium and compared it to their primary tissue counterparts obtained from *A. l. cowlesi* late embryonic venom gland. From organoids, a total of 1,536 cells were sorted, processed using the SORT-seq method (Muraro et al., 2016) and analyzed using the RaceID3 package (Herman et al., 2018). Reads were mapped to the *de novo* assembled *A. l. cowlesi* transcriptome, processed using a newly generated pipeline and filtered for >2,000 transcripts per cell. The 1,092 cells that passed the thresholds displayed a median expression of 10,480 transcript counts per cell (Figures S2A and S2B). K-medoids-based clustering compartmentalized the cells into 12 different cell clusters, as visualized by t-Distributed Stochastic Neighbor Embedding (t-SNE) (Figure 4A). Cells derived from expansion and differentiation medium clustered mostly separately (Figure 4B). Expression of one of the most abundant 3FTxs (*Pr-SNTX*) (Figure S1G) revealed the presence of at least 4 cell clusters producing venom factors (Figure 4C). In line with the bulk transcriptome data, the vast majority of venom-producing cells were derived from differentiated organoids.

Single-cell RNA sequencing of freshly isolated venom gland tissue (using the same pipeline as for the organoid cells) yielded 1,255 cells that passed the same threshold (Figure 4D). Based on their transcriptomic profile, these cells fell into 20 different cell clusters (Figure 4D). Using mammalian markers of cell types expected to be present in glandular organs, we determined the following composition of our dataset: 53% epithelial cells (*EPCAM*, *KRT8*) (Figures 4E and S2C), 27% stromal cells (*COL3A1*), 8% hematopoietic cells (*HEMGN, LYZ*), 7% smooth muscle cells (*ACTA2*), and 4% endothelium (*CDH5*) (Figure S2C). Expression of 3FTx *Pr-SNTX* was highest in two of the cell clusters of epithelial origin (Figure 4F). We also detected strong co-expression of protein disulfide isomerase (*PDI*) with 3FTx variants (*Scutellatus toxin 3*) in the organoids (Figure 4G) as well as in the primary tissue cells (Figure 4H). This enzyme is a key factor to ensure correct disulfide bond folding (Wang and Tsou, 1993), conceivably supporting the disulfide bond-rich structure of three finger toxins. A more detailed analysis of toxin-related gene expression per cluster uncovered that individual venom factors were strongly enriched in separate organoid clusters, suggesting the presence of specialized cells for some of the toxin families (Figure S2D).

We then extracted all 670 epithelial cells from the dataset and performed reclustering (Figure S2E). This resulted in 10 different epithelial subclusters, each enriched for different venom factors. Comparing the heterogeneity in the expression of different toxin classes (3FTx, CRISP, KUN, SVMP, and CTL), we concluded that organoids successfully recapitulate the cellular complexity of venom producing cells *in vivo* (Figure S2F).

Cluster 1 in organoids and cluster 6 in primary tissue comprised cells enriched for transcripts of 3FTx genes (Figure S3A), a subset of these cells additionally expressed Kunitz variants (*KUN*s) (Figure S3B). The cells in cluster 4 (organoids) and cluster 6 and 8 (tissue) were positive for SVMP (Figure S3C). Organoid cells expressing CRISP genes were enriched in cluster 11 and 12; in the tissue these genes were found to be expressed in a larger number of cells enriched in cluster 3 (Figure S3D). Organoid cluster 3 consisted of cells co-expressing CTL and Waprin-related toxins (Figure S3E) (Torres et al., 2003; Ogawa et al., 2005). CTLs have not previously been detected in the *Aspidelaps lubricus* venom proteome and did not form an independent cluster in the tissue dataset (Whiteley et al., 2019).

Cluster 5, containing cells exclusively derived from differentiated organoids, was devoid of any known toxin expression. Comparing this cluster with venom producing clusters 1, 2, 3, and 4, we found these cells to be enriched in extracellular matrix component transcripts such as laminin (*LAMA3*) (Figure 4I). This transcriptomic separation is indicative of two different cellular lineages captured by the organoids, an "epithelial supportive cell" (EP-SUP) fate and a "toxin producing cell" (TOX) fate (Figure S4A). In the complete dataset of venom gland tissue cells, we found clusters 7, 15, and 19 to be enriched in *LAMA3* expression, while these cells expressed much fewer toxin transcripts compared to the other epithelial cells (Figures 4J and S4B). In organoids, as well as tissue, the EP-SUP lineage additionally expressed *CTGF*, *COL7A1*, and *FRZB* (Figures S4C–S4E). Based

(F) Plot of normalized read count of three selected toxins for *N. nivea* and *A. l. cowlesi* organoid bulk mRNA sequencing after 7 days of differentiation. *N. nivea* data generated from bulk RNA sequencing mapped on de *novo A. l. cowlesi* transcriptome (n = 1). *A. l cowlesi* read count from differentiation data (n = 1).
(G) Schematic representation of PCR amplification of *3FTX* coding sequence from cDNA obtained from organoids. Location of forward (F) and reverse (R) primer.
(H) Peptide sequence of *in silico* translated *3FTX* coding sequences of *A. l. cowlesi* and *N. nivea.* Highlighted in red species differences, green arrow conserved disulfide sites. BLASTP hit for best match with proteins in the NCBI database.

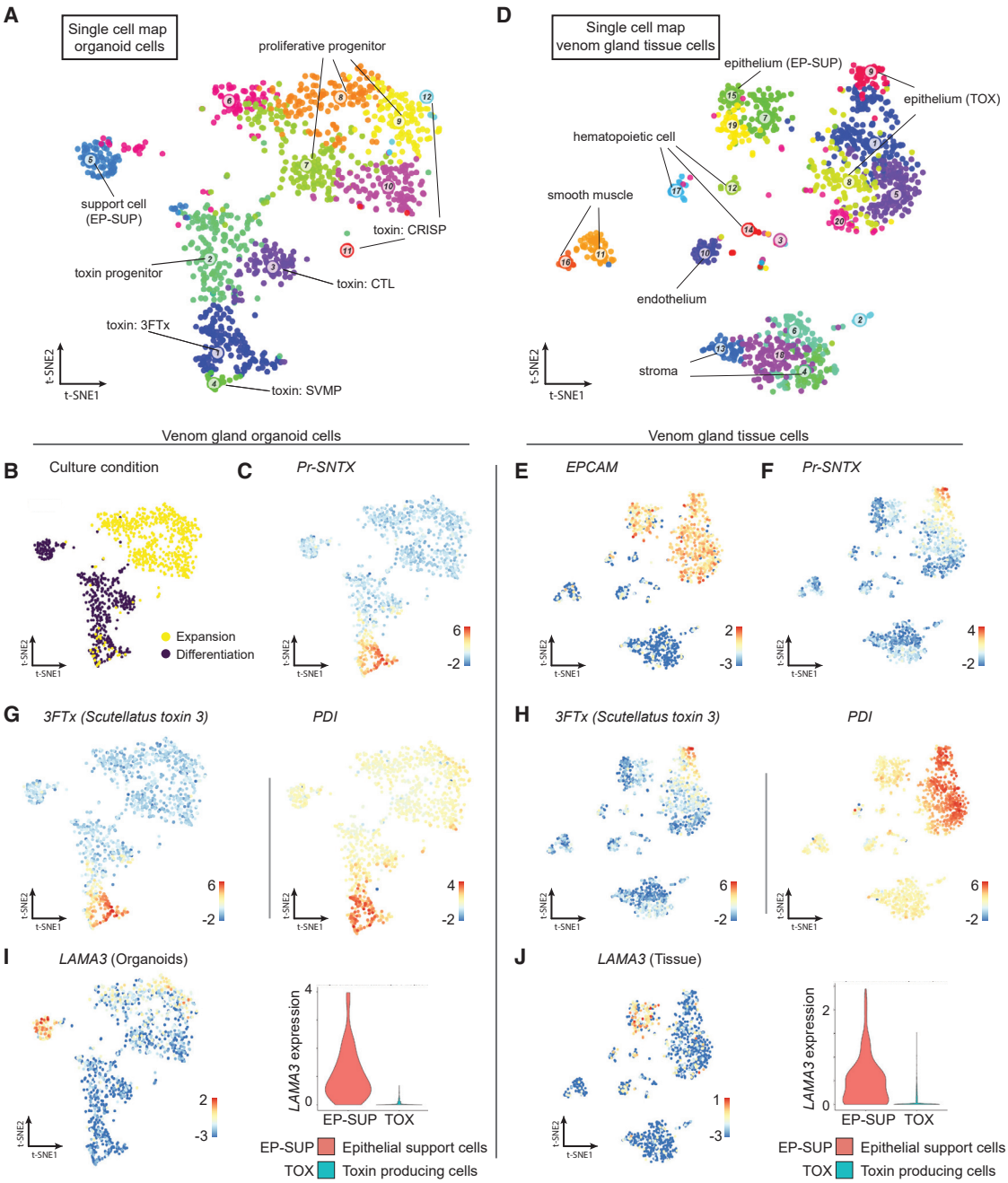

Figure 4. Single-Cell Transcriptome Analysis of Organoids and Primary Tissue Reveals Distinct Venom Gland Cell Types

(A) Single-cell RNA sequencing: clustering of *A. l. cowlesi* venom gland organoid cells (n = 1092) visualized by t-Distributed Stochastic Neighbor-Embedding (t-SNE) map. Colors highlight different clusters (n = 12).

(B) t-SNE map indicating exposure to expansion medium (yellow) or differentiation medium (purple) for 7 days.

(C) Expression level of three-finger toxin *Pr-SNTX* in t-SNE map (color coded logarithmic scale of transcript expression)

(D) Clustering of primary *A. l. cowlesi* venom gland tissue cells (n = 1,255) visualized by t-SNE map. Colors highlight different clusters (n = 20).

(E) Expression level of epithelial cell marker *EPCAM* in t-SNE map (color coded logarithmic scale of transcript expression).

(F) Expression level of three-finger toxin *Pr-SNTX* in t-SNE map (color coded logarithmic scale of transcript expression).

(G and H) Expression levels of selected genes in t-SNE map (color coded logarithmic scale of transcript expression). Left is venom gland organoids cells and right is primary venom gland tissue cells.

(I and J) Expression levels of *LAMA3* in t-SNE map (color coded logarithmic scale of transcript expression) and violin plots visualizing expression levels of cluster-enriched toxins. For both organoid cells (I) and venom gland tissue cells (J) color coded EP-SUP cells (red) and TOX cells (green).

See also Figures S2, S3, S4, and S5.

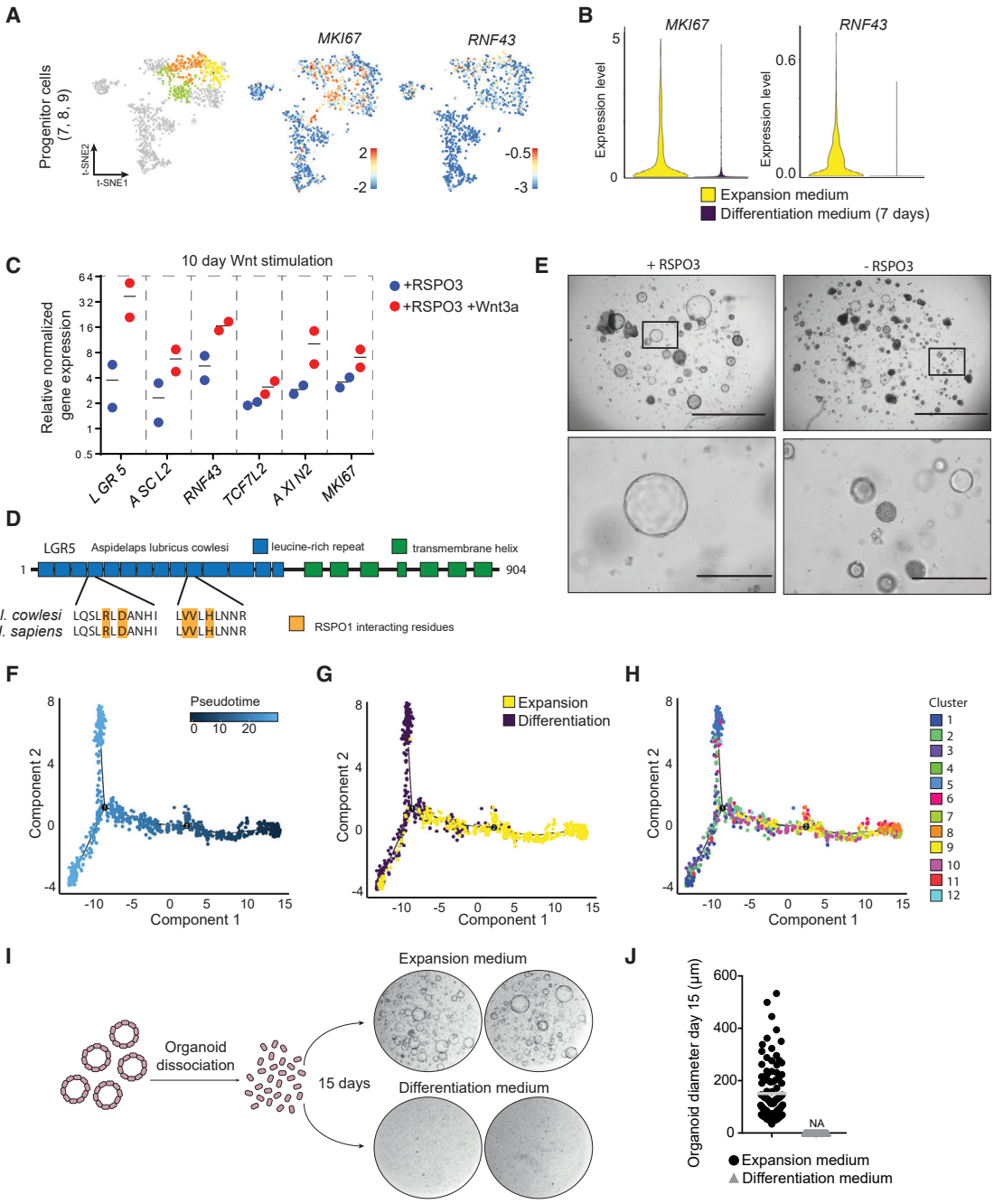

Figure 5. Non-venomous Organoid Cells Include Wnt-Active Proliferating Cells

(A) Expression levels of *MKI67* and *RNF43* in t-SNE map (color coded logarithmic scale of transcript expression).

(B) Violin plot of *MKI67* and *RNF43* expression levels in cells from expansion medium (yellow) or differentiation medium (purple).

(C) Changes in organoid gene expression levels after 10 day Wnt activation (addition of RSPO and RSPO plus exogenous Wnt3a). Expression levels were determined by qPCR and shown relative to "no RSPO and no Wnt3a exposure," normalized to *ACTB*.

(D) Schematic overview of *A. l. cowlesi* LGR5 protein and alignment of R-spondin-interacting residues with the human amino acid sequence.

(E) Representative bright field images of organoids grown for 14 days with (+RSPO3) or without (−RSPO3) R-spondin in culture medium. Scale bars, 2,000 µm (upper panels) and 400 µm (lower panels).

(F) Ordering of cells from single cell sequencing data along a pseudotemporal trajectory using Monocle.

(G) Position of cells exposed to expansion medium (yellow) or differentiation medium (purple) for 7 days along the pseudotemporal trajectory.

(H) Position of cells belonging to the 12 different clusters along the pseudotemporal trajectory.

(legend continued on next page)

on our single cell sequencing of the venom gland tissue, all epithelial lineages/cell types were represented in the organoids. Importantly, marker expression analysis of each of the 12 cell clusters in early and late passage organoids supported the notion that cellular composition of organoids was stable over time in culture (Figure S4F).

Characterization of the Wnt-Activated Proliferative Cells

Having identified the distribution of toxin expression in differentiated cells, we next focused on the expression patterns specific to cell clusters observed under expansion conditions. While some cells in expansion medium clustered together with toxin-expressing cells in clusters 1, 4, 11, and 12, the vast majority fell within the expansion medium-specific clusters 6–10 (Figures 4A and 4B). Cluster 10 was distinct in displaying high expression of phospholipase A2 inhibitor (*PLI*) (Figure S5A), previously described in other snake species as a self-protective mechanism against venom PLA2 toxins (Lima et al., 2011). Expression of *PLI* was also found in epithelial cells from primary tissue (Figure S5B).

Cells in organoid clusters 7, 8, and 9 expressed the proliferation marker Ki-67 (*MKI67*) (Figure 5A). Transcripts for the snake homologs of the mammalian stem cell markers *RNF43* (Koo et al., 2012), *ASCL2* (van der Flier et al., 2009), and *LGR5* (Barker et al., 2007) were enriched in these clusters and were specifically observed under expansion conditions, while being rare in primary tissue (Figures 5A, 5B, and S5C–S5F). This implied these clusters to represent reptilian adult stem/progenitor cells.

Addition of R-spondin 3 enhanced expression of the stem cell markers *LGR5*, *ASCL2*, and *RNF43* together with the well-established Wnt targets *TCF7L2* and *AXIN2*. Supplementation of exogenous Wnt3a further increased expression of these marker genes. As expected, stimulation of the Wnt pathway also induced the proliferation marker *MKI67* (Figure 5C). *A. l. cowlesi* LGR5 shares the same leucine-rich repeats and transmembrane helices with high conservation in the R-spondin interacting residues (R144, D146, V213, V214, and H216) compared to the human protein (Figure 5D) (Chen et al., 2013). Indeed, human R-spondin 3 was found to be essential for organoid expansion (Figures 1D, 5E, and S1B).

The non-epithelial niche is replaced in organoid culture by the addition of defined exogenous growth factors. Using the single-cell sequencing dataset of venom gland tissue, we searched for expression of such secreted factors. We detected the EP-SUP cluster as an epithelial source of *WTN10A* expression (Figure S5G). Stromal cells (clusters 4, 6, 13, and 18) specifically expressed *WNT9A*, *FGF7*, and the BMP-antagonists *CHRD* (Piccolo et al., 1996) and *FSTL1* (Sylva et al., 2011) (Figures S5H–S5K). As expected, transcripts for these proteins with a stromal source *in vivo* were not detected in the organoids.

Pseudotemporal ordering of venom gland organoid cells grown in expansion and differentiation medium using Monocle (Trapnell et al., 2014) was then applied to shed light on the venom gland stem cell hierarchy. Cells from the proliferative progenitor clusters 7, 8, and 9 were placed at the start of the pseudotime axis, in agreement with their stem/progenitor state. A bifurcation was formed by the EP-SUP cells of cluster 5 and TOX cells from clusters 1, 2, 3, and 4 (Figure 5F–5H). To confirm the lack of proliferative and stem cell capacity in the mature clusters (clusters 1–5, Figures 4A and 4B), we differentiated organoids using the growth factor depletion described above. This caused a dramatic reduction in outgrowth and proliferative capacity compared to expansion conditions (Figures 5I and 5J).

Regional Heterogeneity in Toxin Production in the Venom Gland Is Maintained in Organoid Culture

Secretory cells of other mammalian organs, such as the intestine, display regional variation in the types of secreted products. For instance, organoids derived from different regions of the mouse small intestine produce a region-specific repertoire of hormones that is maintained indefinitely *in vitro* (Beumer et al., 2018). We investigated regional heterogeneity in toxin production in the snake venom gland using our organoid culture system. The venom gland of embryonic *A. l. cowlesi* was dissected into a proximal (located near the duct) and a distal part and established region-specific organoids (Figure 6A). After culturing organoids for 1 month (4 passages), we analyzed toxin expression in expansion and differentiation medium by qPCR. We found *CTL* expression to be strongly enriched in "proximal" organoids, whereas "distal" organoids cells predominantly produced *3FTX* and *KUN* toxins (Figure 6B).

Next, we utilized RNA *in situ* hybridization to visualize the expression of these toxins in venom gland tissue. We found a strong enrichment of *CTL* transcripts in the proximal part of the gland, whereas *KUN* was predominantly expressed in the distal tissue, confirming our findings in organoids (Figures 6C, S5L, and S5M). This is in line with a previous report of *CTL* expression in the proximally located accessory gland in the king cobra (Vonk et al., 2013). *CRISP* expression was homogeneous along the proximal-distal axis of the gland, while displaying a bias toward basal over luminal cells (Figure 6C). These data highlighted regional heterogeneity in toxin expression in the snake venom gland (Figure 6D). Long-term maintenance of this phenotype in organoid culture showed this not to be determined by extrinsic (non-epithelial) growth factors.

Venom Gland Organoids Secrete Functionally Active Toxins

To investigate whether the stem-cell-based organoids produced functionally active venom components, we analyzed organoid protein extracts after 7 days of differentiation. The presence of secretory vesicles and the apparent accumulation of proteins in the lumen of organoids suggested significant production of secretory proteins (Figures 2B and 7A). To validate functional translation and secretion of toxins, we generated a fluorescent

(I and J) Schematic overview of experimental setup and representative bright field images of organoid outgrowth in expansion medium and differentiation medium starting from a near-single-cell state. Circular images represent 20 μL BME droplets containing cells/organoids. (J) is quantification of (I). Data points represent individual organoids.
See also Figure S5.

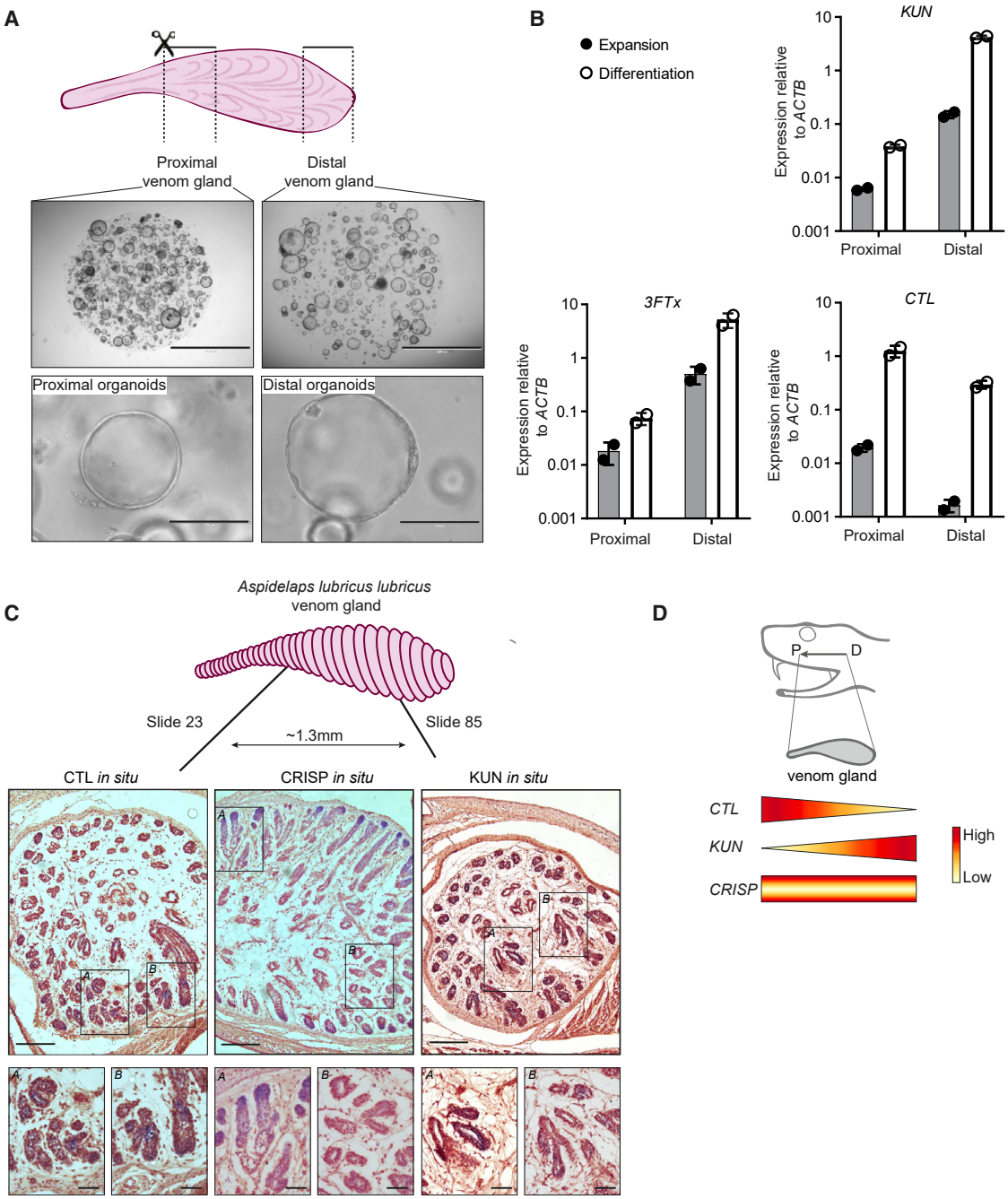

Figure 6. Hard-Wired Regional Heterogeneity in Toxin Expression Is Maintained in Organoids from Proximal and Distal Venom Gland

(A) Schematic representation and bright field images of organoids derived from the proximal and distal region of the *A. l. cowlesi* venom gland. Scale bars, upper panels, 2,000 μm, lower panels, 200 μm.

(B) Gene expression of toxins (*KUN*, *3FTX*, and *CTL*) in proximal and distal organoid lines (passage 4) exposed to expansion medium or differentiation medium (7 days). Expression levels were determined by qPCR shown relative to *ACTB*. Data points represent biological replicates.

(C) Schematic representation of venom gland sections from proximal to distal. BM-purple stain of *in situ* hybridization for CTL (slide 23), CRISP, and KUN (slide 85) in *A. l. cowlesi* venom gland tissue. Scale bars, upper panels, 200 μm, lower panels, 50 μm.

(D) Schematic overview of regional heterogeneity in venom gland toxin expression: CTL expression proximal, KUN expression distal, and CRISP expression along the proximal-distal axis on the basal side.

See also Figure S5.

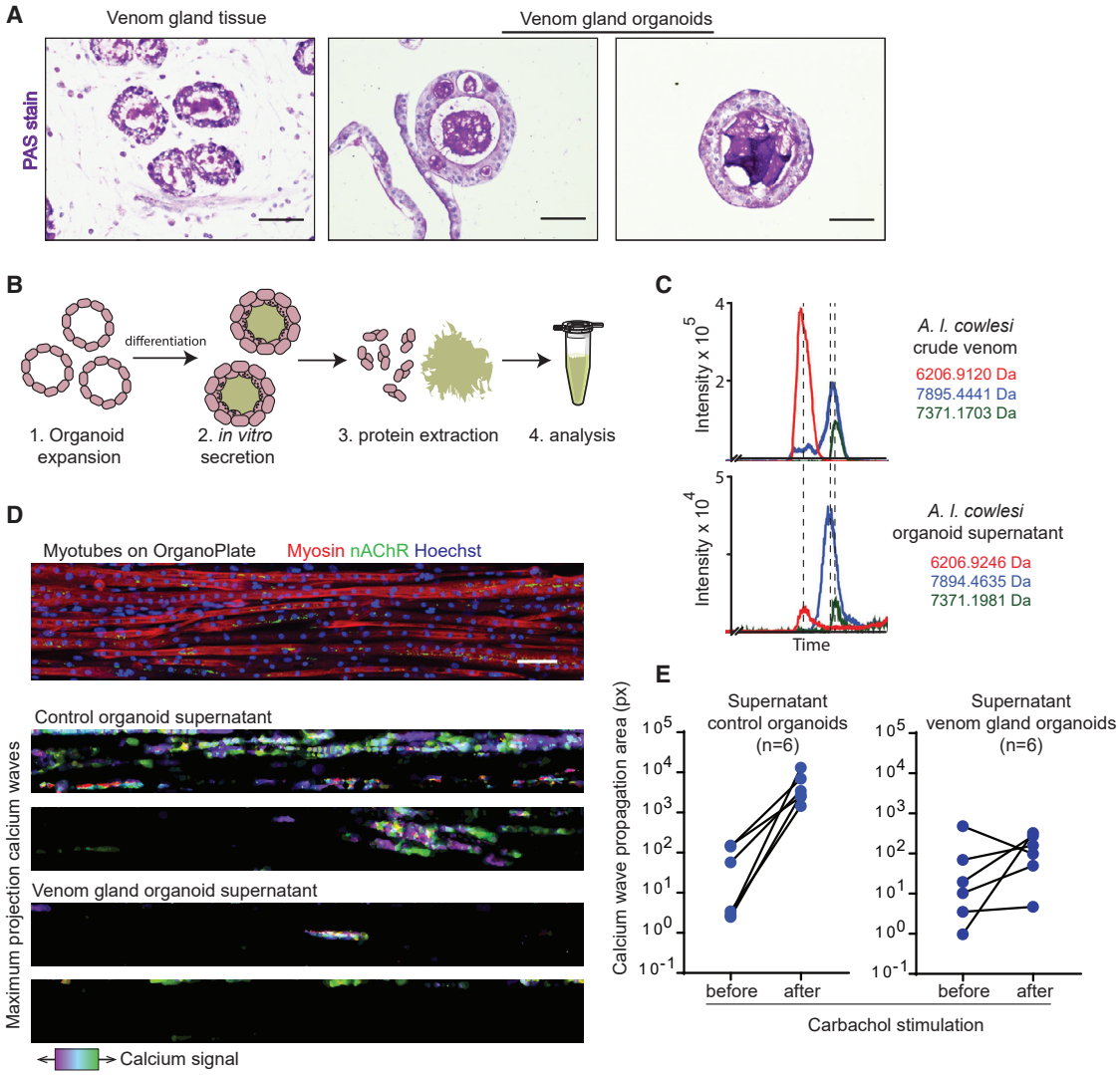

Figure 7. Organoids Produce Biologically Active Toxins

(A) Luminal accumulation of secreted proteins was determined using periodic acid-Schiff (PAS) staining in late embryonic venom gland tissue and organoids. Scale bars, 50 μm.

(B) Schematic representation of organoid extraction. Organoids were expanded for four days and then subjected to a seven-day differentiation protocol. In PBS, the lumen was opened using mechanical shearing and cells disrupted using sonication. Cellular debris was pelleted by centrifugation and supernatant collected for analysis.

(C) Direct comparison of *A. l. cowlesi* crude venom (upper panel) with organoid extract (lower panel) using liquid chromatography-mass spectrometry (LC-MS) identifies three overlapping products. Ion-chromatogram displays signal intensity (y axis) over retention time in minutes (x axis) with indicated mass per trace.

(D) Immunofluorescence staining of C2C12 myotubes in OrganoPlate, myosin (red), nAChR (green), and Hoechst (blue) (upper panel). Scale bar, 100 μm. The calcium wave propagation was imaged before and after exposure to different supernatants in chips. Maximum projected images depict the total calcium signal over all image frames after carbachol stimulation, in which purple reflects activity to the left and green to the right (lower panels).

(E) Quantification of (D). The total calcium signal was calculated before and after carbachol stimulation based on total fluorescent signal. The venom gland organoid supernatant blunts the induction of calcium sparks. Data points represent biological replicates.

See also Figures S6 and S7.

3FTx reporter organoid line. Using CRISPR-HOT (J.B., H.C., B. Artegiani, and D. Hendriks, unpublished data), we tagged one of the endogenous 3FTxs (*NTX4*) with a fluorescent protein (mNeon-Green) (Figure S6A). We detected the green fluorescent fusion protein inside the cells of the organoids and accumulating in the lumen (Figure S6A).

We also directly compared organoid extract (Figure 7B) with *A. l. cowlesi* crude venom using liquid chromatography-mass spectrometry (LC-MS). This revealed three main peaks between 6–8 kDa of near identical mass between the two samples (Figure 7C). Tryptic digest analysis of these peptides yielded patterns compatible with

several venom-related proteins such as 3FTx and CRISP (Figure S6B).

Snake venom neurotoxins are described to act primarily on acetylcholine receptors (nAChR and mAChR) (Nirthanan and Gwee, 2004; Karlsson et al., 2000). As an initial assessment of the biological activity of organoid-secreted venom peptides, we exposed murine muscle cultures (endogenously expressing the nAChR) to the organoid supernatant and recorded signal propagation using calcium imaging in an OrganoPlate (Trietsch et al., 2017) (Figures 7D and S6C–S6F). This organ-on-a-chip platform allows live cell imaging during venom exposure in 96 independent mature muscle cultures per plate. The venom peptides derived from differentiated organoids abolished the stimulatory effect of the acetylcholine receptor agonist carbachol on muscle cells, as did the positive control alpha-bungarotoxin (α-BTX). Supernatant from non-venom producing (human) organoids did not inhibit calcium wave propagation after addition of carbachol (Figures 7E and S6G–S6I).

In a similar set-up, we exposed rat cortical neurons grown on microelectrode array (MEA) plates to organoid supernatant and recorded neuronal activity (Figure S7A). Upon acute exposure, we noticed a marked increase in neuronal activity, following a similar trend observed with recombinant alpha-bungarotoxin (Figures S7B–S7D). This occurred most likely through an antagonistic effect on inhibitory GABAa-receptors (McCann et al., 2006), without affecting neuronal cell viability (Figures S7E–S7G).

DISCUSSION

We report the establishment of reptilian adult stem-cell-based organoids. Using a mammalian niche growth factor cocktail, these cells can be expanded seemingly indefinitely. The ability to culture venom gland epithelial cells over long periods of time represents a platform for a comprehensive understanding of the biology of the venom gland and the various venom constituents. Short-term cultures of different Viperidae snakes have previously been reported, such as explants of *Bothrops jararaca* (Carneiro et al., 2006; Yamanouye et al., 2006), suspension cultures of *Bitis gabonica* (Sells et al., 1989), and unpolarized two-dimensional cell lines of *Crotalus durissus terrificus* (Duarte et al., 1999). The venom gland organoid cultures provides advantages in structural conservation (Figure 1C), cellular heterogeneity (Figure 4), regional heterogeneity (Figure 6), long-term expansion (Figures 1B and 3A), genetic modifiability (Figures S1E and S6A), and broad applicability across snake species (Figure S1A). With a *de novo*-generated transcriptome of *A. l. cowlesi*, we demonstrate that the venom gland organoid cells produce a diverse spectrum of venom factors over many passages (Figure 2).

Previous mammalian organoid cultures have highlighted the importance of Wnt-driven stem cell maintenance *in vitro* (Clevers, 2016). Indeed, we identify a proliferative population of cells in the venom gland organoids that is defined by the expression of the snake homologs of established Wnt-driven stem cell genes of mammalian epithelia: LGR5 (Barker et al., 2007), ASCL2 (van der Flier et al., 2009), and RNF43 (Koo et al., 2012). The importance of R-spondin in reptilian cell proliferation highlights the critical role and a high level of conservation of the Wnt pathway in ASC biology. We believe that the culture conditions used here may be widely applicable to vertebrate species.

While a divergent composition of snake venoms between species, and even between and within individuals, is well-established (Casewell et al., 2014; Augusto-de-Oliveira et al., 2016; Zancolli et al., 2019), the cellular heterogeneity underlying the production of individual toxins is not well described. Initial attempts at characterizing the cell types of the snake venom gland through electron microscopy has resulted in the morphological identification of at least 4 cell types, of which columnar epithelial cells containing granules have been suggested to be the main source of venom production and secretion (Mackessy, 1991). The amount and type of venom detectable in individual cells is influenced by the secretory cycle, referring to temporal dynamics in venom production and secretion (Taylor et al., 1986; Shaham and Kochva, 1969). A previous study identified heterogeneity in the binding of single-component antibodies to secretory granules and attributed this mainly to the secretory cycle-dependent production of toxins rather than cellular heterogeneity of the venom gland (Taylor et al., 1986).

Our data describe cellular heterogeneity in the venom gland epithelium at the level of transcription. Gene expression profiling at single cell resolution of both organoids and primary tissue uncovers the coincident expression of characteristic groups of toxins by individual cell types. Future studies may use venom gland organoids to dissect the stimuli and timing of venom production and secretion. The ability to indefinitely expand these organoids and repeatedly harvest venom supernatants in a highly defined environment may help overcome hurdles posed by the significant variation in snake venom composition.

Finally, the current study opens new avenues for bioprospecting of snake venom components and may be developed into a production platform for (modified) snake venom, allowing novel therapeutic strategies to tackle snakebite.

STAR★METHODS

Detailed methods are provided in the online version of this paper and include the following:

- KEY RESOURCES TABLE
- LEAD CONTACT AND MATERIALS AVAILABILITY
- EXPERIMENTAL MODEL AND SUBJECT DETAILS
  - Snakes
  - Venom gland organoid cultures
  - C2C12 cell line
  - Primary rat cortical neurons
- METHOD DETAILS
  - Venom gland isolation
  - Venom gland organoid cultures
  - Immunohistochemistry and imaging
  - Electron microscopic analysis
  - Organoid protein extraction
  - Liquid chromatography–mass spectrometry and Mascot database search
  - Myotube cultures
  - Calcium imaging
  - MEA recordings rat cortical neurons

- Bulk and single cell RNA sequencing
- Bulk and single cell RNA sequencing analysis

- QUANTIFICATION AND STATISTICAL ANALYSIS
- DATA AND CODE AVAILABILITY

SUPPLEMENTAL INFORMATION

Supplemental Information can be found online at https://doi.org/10.1016/j.cell.2019.11.038.

ACKNOWLEDGMENTS

We thank Reinier van der Linden for flow cytometry assistance; Benedetta Artegiani and Delilah Hendriks for generation of CRISPR-HOT technology and assistance in applying it to snake venom gland organoids; Anko de Graaff and the Hubrecht Imaging Centre (HIC) for microscopy assistance; BaseClear B.V. for bulk mRNA sequencing and *de novo* transcriptome assembly; Bas Ponsioen for providing the lentiviral H2B-RFP construct; Single Cell Discoveries for the provided single-cell sequencing service and support; Jeremie Tai-A-Pin and Harold van der Ploeg for donating venom gland material to this study; and Sebastiaan Voskuil, Edwin Boel, Marc Bonten, and Frank Driehuis for advice regarding antibiotic treatments. X.M.S. was supported by ALS Foundation Netherlands. N.R.C. was supported by a Sir Henry Dale Fellowship (200517/Z/16/Z) jointly funded by the Wellcome Trust and the Royal Society.

AUTHOR CONTRIBUTIONS

Y.P., J.P., J.B., and H.C. conceptualized the project, designed the experiments, interpreted the results, and wrote the manuscript. H.B. and J. Korving performed immunohistochemistry experiments. J.P., B.d.B., A.v.O., M.C.H., and H.J.G.S. performed bulk and single-cell mRNA sequencing analysis on *de novo* transcriptome. Y.E.B.-E. assisted with FACS experiments. C.L.I., W.J.v.d.W., and P.J.P. performed transmission electron microscopy. M.A.G.d.B. performed *in situ* hybridization experiments. R.L.v.I. and A.C.R. generated immunofluorescent images. J.S. and J. Kool performed mass spectrometry analysis. S.A., T.D.K., and N.R.C. performed toxin gene expression analysis on bulk RNA sequencing data. N.R.W., X.M.S., and T.O. performed and analyzed toxicity tests on Mimetas OrganoPlate. H.M.K., F.J.V., and M.K.R. assisted in initializing the project and provided access to venom gland tissue. R.H.S.W. and R.G.D.M.v.K performed and analyzed toxicity tests on rat cortical neurons in MEA plates. W.G. and N.R.C. provided venom gland tissue.

DECLARATION OF INTERESTS

H.C. is inventor on several patents related to organoid technology; his full disclosure is given at https://www.uu.nl/staff/JCClevers/. N.R.W. and T.O. are employees of MIMETAS BV, the Netherlands, which is marketing the OrganoPlate. OrganoPlate is a registered trademark of MIMETAS.

Received: April 19, 2019
Revised: October 29, 2019
Accepted: November 27, 2019
Published: January 23, 2020

REFERENCES

Ainsworth, S., Slagboom, J., Alomran, N., Pla, D., Alhamdi, Y., King, S.I., Bolton, F.M.S., Gutierrez, J.M., Vonk, F.J., Toh, C.H., et al. (2018). The paraspecific neutralisation of snake venom induced coagulopathy by antivenoms. Commun. Biol. *1*, 34.

Artegiani, B., and Clevers, H. (2018). Use and application of 3D-organoid technology. Hum. Mol. Genet. *27* (R2), R99–R107.

Augusto-de-Oliveira, C., Stuginski, D.R., Kitano, E.S., Andrade-Silva, D., Liberato, T., Fukushima, I., Serrano, S.M., and Zelanis, A. (2016). Dynamic Rearrangement in Snake Venom Gland Proteome: Insights into Bothrops jararaca Intraspecific Venom Variation. J. Proteome Res. *15*, 3752–3762.

Barker, N., van Es, J.H., Kuipers, J., Kujala, P., van den Born, M., Cozijnsen, M., Haegebarth, A., Korving, J., Begthel, H., Peters, P.J., and Clevers, H. (2007). Identification of stem cells in small intestine and colon by marker gene Lgr5. Nature *449*, 1003–1007.

Beumer, J., Artegiani, B., Post, Y., Reimann, F., Gribble, F., Nguyen, T.N., Zeng, H., Van den Born, M., Van Es, J.H., and Clevers, H. (2018). Enteroendocrine cells switch hormone expression along the crypt-to-villus BMP signalling gradient. Nat. Cell Biol. *20*, 909–916.

Bolhaqueiro, A.C.F., van Jaarsveld, R.H., Ponsioen, B., Overmeer, R.M., Snippert, H.J., and Kops, G.J.P.L. (2018). Live imaging of cell division in 3D stem-cell organoid cultures. Methods Cell Biol. *145*, 91–106.

Butler, A., Hoffman, P., Smibert, P., Papalexi, E., and Satija, R. (2018). Integrating single-cell transcriptomic data across different conditions, technologies, and species. Nat. Biotechnol. *36*, 411–420.

Carneiro, S.M., Zablith, M.B., Kerchove, C.M., Moura-da-Silva, A.M., Quissell, D.O., Markus, R.P., and Yamanouye, N. (2006). Venom production in long-term primary culture of secretory cells of the Bothrops jararaca venom gland. Toxicon *47*, 87–94.

Casewell, N.R., Wagstaff, S.C., Wüster, W., Cook, D.A., Bolton, F.M., King, S.I., Pla, D., Sanz, L., Calvete, J.J., and Harrison, R.A. (2014). Medically important differences in snake venom composition are dictated by distinct postgenomic mechanisms. Proc. Natl. Acad. Sci. USA *111*, 9205–9210.

Chen, P.H., Chen, X., Lin, Z., Fang, D., and He, X. (2013). The structural basis of R-spondin recognition by LGR5 and RNF43. Genes Dev. *27*, 1345–1350.

Clark, G.C., Casewell, N.R., Elliott, C.T., Harvey, A.L., Jamieson, A.G., Strong, P.N., and Turner, A.D. (2019). Friends or Foes? Emerging Impacts of Biological Toxins. Trends Biochem. Sci. *44*, 365–379.

Clevers, H. (2016). Modeling Development and Disease with Organoids. Cell *165*, 1586–1597.

de Lau, W., Barker, N., Low, T.Y., Koo, B.K., Li, V.S., Teunissen, H., Kujala, P., Haegebarth, A., Peters, P.J., van de Wetering, M., et al. (2011). Lgr5 homologues associate with Wnt receptors and mediate R-spondin signalling. Nature *476*, 293–297.

Dekkers, J.F., Wiegerinck, C.L., de Jonge, H.R., Bronsveld, I., Janssens, H.M., de Winter-de Groot, K.M., Brandsma, A.M., de Jong, N.W., Bijvelds, M.J., Scholte, B.J., et al. (2013). A functional CFTR assay using primary cystic fibrosis intestinal organoids. Nat. Med. *19*, 939–945.

Dekkers, J.F., Alieva, M., Wellens, L.M., Ariese, H.C.R., Jamieson, P.R., Vonk, A.M., Amatngalim, G.D., Hu, H., Oost, K.C., Snippert, H.J.G., et al. (2019). High-resolution 3D imaging of fixed and cleared organoids. Nat. Protoc. *14*, 1756–1771.

Dingemans, M.M., Schütte, M.G., Wiersma, D.M., de Groot, A., van Kleef, R.G., Wijnolts, F.M., and Westerink, R.H. (2016). Chronic 14-day exposure to insecticides or methylmercury modulates neuronal activity in primary rat cortical cultures. Neurotoxicology *57*, 194–202.

Duarte, M.M., Montes de Oca, H., Diniz, C.R., and Fortes-Dias, C.L. (1999). Primary culture of venom gland cells from the South American rattlesnake (Crotalus durissus terrificus). Toxicon *37*, 1673–1682.

Fatehullah, A., Tan, S.H., and Barker, N. (2016). Organoids as an in vitro model of human development and disease. Nat. Cell Biol. *18*, 246–254.

Fox, J.W., and Serrano, S.M. (2008). Exploring snake venom proteomes: multifaceted analyses for complex toxin mixtures. Proteomics *8*, 909–920.

Fry, B.G., Vidal, N., van der Weerd, L., Kochva, E., and Renjifo, C. (2009). Evolution and diversification of the Toxicofera reptile venom system. J. Proteomics *72*, 127–136.

Gehart, H., van Es, J.H., Hamer, K., Beumer, J., Kretzschmar, K., Dekkers, J.F., Rios, A., and Clevers, H. (2019). Identification of Enteroendocrine Regulators by Real-Time Single-Cell Differentiation Mapping. Cell *176*, 1158–1173.

Grün, D., Lyubimova, A., Kester, L., Wiebrands, K., Basak, O., Sasaki, N., Clevers, H., and van Oudenaarden, A. (2015). Single-cell messenger RNA sequencing reveals rare intestinal cell types. Nature *525*, 251–255.

Gutierrez, J.M., and Lomonte, B. (2013). Phospholipases A2: unveiling the secrets of a functionally versatile group of snake venom toxins. Toxicon *62*, 27–39.

Gutiérrez, J.M., Calvete, J.J., Habib, A.G., Harrison, R.A., Williams, D.J., and Warrell, D.A. (2017). Snakebite envenoming. Nat. Rev. Dis. Primers *3*, 17063.

Haas, B.J., Papanicolaou, A., Yassour, M., Grabherr, M., Blood, P.D., Bowden, J., Couger, M.B., Eccles, D., Li, B., Lieber, M., et al. (2013). De novo transcript sequence reconstruction from RNA-seq using the Trinity platform for reference generation and analysis. Nat. Protoc. *8*, 1494–1512.

Harvey, A.L. (2001). Twenty years of dendrotoxins. Toxicon *39*, 15–26.

Hashimshony, T., Senderovich, N., Avital, G., Klochendler, A., de Leeuw, Y., Anavy, L., Gennert, D., Li, S., Livak, K.J., Rozenblatt-Rosen, O., et al. (2016). CEL-Seq2: sensitive highly-multiplexed single-cell RNA-Seq. Genome Biol. *17*, 77.

Herman, J.S., Sagar, and Grün, D. (2018). FateID infers cell fate bias in multipotent progenitors from single-cell RNA-seq data. Nat. Methods *15*, 379–386.

Izidoro, L.F., Sobrinho, J.C., Mendes, M.M., Costa, T.R., Grabner, A.N., Rodrigues, V.M., da Silva, S.L., Zanchi, F.B., Zuliani, J.P., Fernandes, C.F., et al. (2014). Snake venom L-amino acid oxidases: trends in pharmacology and biochemistry. BioMed Res. Int. *2014*, 196754.

Karlsson, E., Jolkkonen, M., Mulugeta, E., Onali, P., and Adem, A. (2000). Snake toxins with high selectivity for subtypes of muscarinic acetylcholine receptors. Biochimie *82*, 793–806.

Kochva, E. (1987). The origin of snakes and evolution of the venom apparatus. Toxicon *25*, 65–106.

Koo, B.K., Spit, M., Jordens, I., Low, T.Y., Stange, D.E., van de Wetering, M., van Es, J.H., Mohammed, S., Heck, A.J., Maurice, M.M., and Clevers, H. (2012). Tumour suppressor RNF43 is a stem-cell E3 ligase that induces endocytosis of Wnt receptors. Nature *488*, 665–669.

Lima, R.M., Estevao-Costa, M.I., Junqueira-de-Azevedo, I.L., Ho, P.L., Diniz, M.R., and Fortes-Dias, C.L. (2011). Phospholipase A2 inhibitors (betaPLIs) are encoded in the venom glands of Lachesis muta (Crotalinae, Viperidae) snakes. Toxicon *57*, 172–175.

Mackessy, S.P. (1991). Morphology and ultrastructure of the venom glands of the northern pacific rattlesnake Crotalus viridis oreganus. J. Morphol. *208*, 109–128.

Maimets, M., Rocchi, C., Bron, R., Pringle, S., Kuipers, J., Giepmans, B.N., Vries, R.G., Clevers, H., de Haan, G., van Os, R., and Coppes, R.P. (2016). Long-Term In Vitro Expansion of Salivary Gland Stem Cells Driven by Wnt Signals. Stem Cell Reports *6*, 150–162.

McCann, C.M., Bracamontes, J., Steinbach, J.H., and Sanes, J.R. (2006). The cholinergic antagonist alpha-bungarotoxin also binds and blocks a subset of GABA receptors. Proc. Natl. Acad. Sci. USA *103*, 5149–5154.

Millers, E.K., Trabi, M., Masci, P.P., Lavin, M.F., de Jersey, J., and Guddat, L.W. (2009). Crystal structure of textilinin-1, a Kunitz-type serine protease inhibitor from the venom of the Australian common brown snake (Pseudonaja textilis). FEBS J. *276*, 3163–3175.

Muraro, M.J., Dharmadhikari, G., Grun, D., Groen, N., Dielen, T., Jansen, E., van Gurp, L., Engelse, M.A., Carlotti, F., de Koning, E.J., et al. (2016). A Single-Cell Transcriptome Atlas of the Human Pancreas. Cell Syst. *3*, 385–394.

Nicolas, J., Hendriksen, P.J., van Kleef, R.G., de Groot, A., Bovee, T.F., Rietjens, I.M., and Westerink, R.H. (2014). Detection of marine neurotoxins in food safety testing using a multielectrode array. Mol. Nutr. Food Res. *58*, 2369–2378.

Nirthanan, S., and Gwee, M.C. (2004). Three-finger alpha-neurotoxins and the nicotinic acetylcholine receptor, forty years on. J. Pharmacol. Sci. *94*, 1–17.

Ogawa, T., Chijiwa, T., Oda-Ueda, N., and Ohno, M. (2005). Molecular diversity and accelerated evolution of C-type lectin-like proteins from snake venom. Toxicon *45*, 1–14.

Piccolo, S., Sasai, Y., Lu, B., and De Robertis, E.M. (1996). Dorsoventral patterning in Xenopus: inhibition of ventral signals by direct binding of chordin to BMP-4. Cell *86*, 589–598.

Richter, K., Haslbeck, M., and Buchner, J. (2010). The heat shock response: life on the verge of death. Mol. Cell *40*, 253–266.

Sato, T., Vries, R.G., Snippert, H.J., van de Wetering, M., Barker, N., Stange, D.E., van Es, J.H., Abo, A., Kujala, P., Peters, P.J., and Clevers, H. (2009). Single Lgr5 stem cells build crypt-villus structures in vitro without a mesenchymal niche. Nature *459*, 262–265.

Sato, T., Stange, D.E., Ferrante, M., Vries, R.G., Van Es, J.H., Van den Brink, S., Van Houdt, W.J., Pronk, A., Van Gorp, J., Siersema, P.D., and Clevers, H. (2011). Long-term expansion of epithelial organoids from human colon, adenoma, adenocarcinoma, and Barrett's epithelium. Gastroenterology *141*, 1762–1772.

Schindelin, J., Arganda-Carreras, I., Frise, E., Kaynig, V., Longair, M., Pietzsch, T., Preibisch, S., Rueden, C., Saalfeld, S., Schmid, B., et al. (2012). Fiji: an open-source platform for biological-image analysis. Nat. Methods *9*, 676–682.

Sells, P.G., Hommel, M., and Theakston, R.D. (1989). Venom production in snake venom gland cells cultured in vitro. Toxicon *27*, 1245–1249.

Shaham, N., and Kochva, E. (1969). Localization of venom antigens in the venom gland of Vipera plaestinae using a fluorescent-antibody technique. Toxicon *6*, 263–268.

Slagboom, J., Kool, J., Harrison, R.A., and Casewell, N.R. (2017). Haemotoxic snake venoms: their functional activity, impact on snakebite victims and pharmaceutical promise. Br. J. Haematol. *177*, 947–959.

Sylva, M., Li, V.S., Buffing, A.A., van Es, J.H., van den Born, M., van der Velden, S., Gunst, Q., Koolstra, J.H., Moorman, A.F., Clevers, H., and van den Hoff, M.J. (2011). The BMP antagonist follistatin-like 1 is required for skeletal and lung organogenesis. PLoS ONE *6*, e22616.

Taylor, D., Iddon, D., Sells, P., Semoff, S., and Theakston, R.D. (1986). An investigation of venom secretion by the venom gland cells of the carpet viper (Echis carinatus). Toxicon *24*, 651–659.

Torres, A.M., Wong, H.Y., Desai, M., Moochhala, S., Kuchel, P.W., and Kini, R.M. (2003). Identification of a novel family of proteins in snake venoms. Purification and structural characterization of nawaprin from Naja nigricollis snake venom. J. Biol. Chem. *278*, 40097–40104.

Trapnell, C., Cacchiarelli, D., Grimsby, J., Pokharel, P., Li, S., Morse, M., Lennon, N.J., Livak, K.J., Mikkelsen, T.S., and Rinn, J.L. (2014). The dynamics and regulators of cell fate decisions are revealed by pseudotemporal ordering of single cells. Nat. Biotechnol. *32*, 381–386.

Trietsch, S.J., Naumovska, E., Kurek, D., Setyawati, M.C., Vormann, M.K., Wilschut, K.J., Lanz, H.L., Nicolas, A., Ng, C.P., Joore, J., et al. (2017). Membrane-free culture and real-time barrier integrity assessment of perfused intestinal epithelium tubes. Nat. Commun. *8*, 262.

Tsetlin, V.I. (2015). Three-finger snake neurotoxins and Ly6 proteins targeting nicotinic acetylcholine receptors: pharmacological tools and endogenous modulators. Trends Pharmacol. Sci. *36*, 109–123.

Tukker, A.M., Wijnolts, F.M.J., de Groot, A., and Westerink, R.H.S. (2018). Human iPSC-derived neuronal models for in vitro neurotoxicity assessment. Neurotoxicology *67*, 215–225.

van der Flier, L.G., van Gijn, M.E., Hatzis, P., Kujala, P., Haegebarth, A., Stange, D.E., Begthel, H., van den Born, M., Guryev, V., Oving, I., et al. (2009). Transcription factor achaete scute-like 2 controls intestinal stem cell fate. Cell *136*, 903–912.

Vonk, F.J., Casewell, N.R., Henkel, C.V., Heimberg, A.M., Jansen, H.J., McCleary, R.J., Kerkkamp, H.M., Vos, R.A., Guerreiro, I., Calvete, J.J., et al. (2013). The king cobra genome reveals dynamic gene evolution and adaptation in the snake venom system. Proc. Natl. Acad. Sci. USA *110*, 20651–20656.

Wang, C.C., and Tsou, C.L. (1993). Protein disulfide isomerase is both an enzyme and a chaperone. FASEB J. *7*, 1515–1517.

Wevers, N.R., Kasi, D.G., Gray, T., Wilschut, K.J., Smith, B., van Vught, R., Shimizu, F., Sano, Y., Kanda, T., Marsh, G., et al. (2018). A perfused human blood-brain barrier on-a-chip for high-throughput assessment of barrier function and antibody transport. Fluids Barriers CNS *15*, 23.

Whiteley, G., Casewell, N.R., Pla, D., Quesada-Bernat, S., Logan, R.A.E., Bolton, F.M.S., Wagstaff, S.C., Gutiérrez, J.M., Calvete, J.J., and Harrison, R.A. (2019). Defining the pathogenic threat of envenoming by

South African shield-nosed and coral snakes (genus Aspidelaps), and revealing the likely efficacy of available antivenom. J. Proteomics *198*, 186–198.

Yamanouye, N., Kerchove, C.M., Moura-da-Silva, A.M., Carneiro, S.M., and Markus, R.P. (2006). Long-term primary culture of secretory cells of Bothrops jararaca venom gland for venom production in vitro. Nat. Protoc. *1*, 2763–2766.

Yamazaki, Y., and Morita, T. (2004). Structure and function of snake venom cysteine-rich secretory proteins. Toxicon *44*, 227–231.

Zancolli, G., Calvete, J.J., Cardwell, M.D., Greene, H.W., Hayes, W.K., Hegarty, M.J., Herrmann, H.W., Holycross, A.T., Lannutti, D.I., Mulley, J.F., et al. (2019). When one phenotype is not enough: divergent evolutionary trajectories govern venom variation in a widespread rattlesnake species. Proc. Biol. Sci. *286*, 20182735.

STAR★METHODS

KEY RESOURCES TABLE

REAGENT or RESOURCE	SOURCE	IDENTIFIER
Antibodies		
Anti-β-catenin	Santa Cruz	Cat # sc-7199; RRID: AB_634603
Anti-β-Tubulin	Santa Cruz	Cat # sc-9104; RRID: AB_2241191
Alexa Fluor 647 Phalloidin	Thermo Scientific	Cat # A22287; RRID: AB_2620155
Anti-Myosin	DSHB	Cat # A4.1025; RRID: AB_528356
Anti-Desmin	Abcam	Cat # ab8470; RRID: AB_306577
Anti-Dystrophin	Abcam	Cat # ab15277; RRID: AB_301813
Alexa Fluor 555 Goat anti-Mouse IgG (H+L)	Thermo Scientific	Cat # A21422; RRID: AB_141822
Alexa Fluor 647 Goat anti-Mouse IgG (H+L)	Thermo Scientific	Cat # A21236; RRID: AB_141725
CF 647 Donkey anti-Rabbit IgG (H+L)	Sigma-Aldrich	Cat # SAB4600177
Alexa Fluor Plus 555 Goat anti-Rabbit IgG (H+L)	Thermo Scientific	Cat # A32732; RRID: AB_2633281
α-Bungarotoxin, Alexa Fluor 488 conjugate	Thermo Scientific	Cat # B13422
Biological Samples		
Crotalus atrox venom glands	Natural Toxins Research Center	tamuk.edu
Echis ocellatus venom glands	Liverpool School of Tropical Medicine	N/A
Deinagkistrodon acutus venom glands	Liverpool School of Tropical Medicine	N/A
Naja pallida venom glands	SERPO	N/A
Bitis arietans venom glands	SERPO	N/A
Naja nivea venom glands	SERPO	N/A
Naja atra venom glands	Local breeder	N/A
Naja annulifera venom glands	Local breeder	N/A
Aspidelaps lubricus cowlesi venom glands	Local breeder	N/A
Wistar outbred rat	Envigo	N/A
Chemicals, Peptides, and Recombinant Proteins		
Advanced DMEM/F12	Thermo Scientific	12634-010
B-27 Supplement	Thermo Scientific	17504044
GlutaMAX	Thermo Scientific	35050061
HEPES	Thermo Scientific	15630080
Penicillin-Streptomycin	Thermo Scientific	15140122
Wnt conditioned medium	In-house production	N/A
Noggin conditioned medium	U-Protein Express	Custom order
R-spondin conditioned medium	U-Protein Express	Custom order
N-Acetyl-L-cysteine	Sigma-Aldrich	A9165
Nicotinamide	Sigma-Aldrich	N0636
Human EGF	Peprotech	AF-100-15
A83-01	Tocris	2939
Prostaglandin E2	Tocris	2296
Forskolin	Tocris	1099
Gastrin I	Tocris	3006
Human FGF-10	Peprotech	100-26
Y-27632 dihydrochloride	Abmole	M1817
Primocin	Invivogen	ant-pm-2

(*Continued on next page*)

Continued

REAGENT or RESOURCE	SOURCE	IDENTIFIER
Gentamicin	Sigma-Aldrich	G1397
Ciprofloxacin	Sigma-Aldrich	17850
Erythromycin	Sigma-Aldrich	E5389
Azithromycin dihydrate	Sigma-Aldrich	PZ0007
Collagenase from Clostridium histolyticum	Sigma-Aldrich	C9407
Basement Membrane Extract (BME), Growth Factor Reduced, Type 2	R&D Systems	3533-001-02
Matrigel Growth Factor Reduced	Corning	356231
DAPI	Thermo Scientific	D1306
Hoechst 33342	Thermo Scientific	H3570
Cell Recovery Solution	Corning	354253
Formaldehyde solution 4%	Sigma-Aldrich	1.00496
Fetal Bovine Serum	Thermo Scientific	16140071
Horse Serum	Thermo Scientific	26050070
Insulin solution human	Sigma-Aldrich	I9278
Cytosine β-D-arabinofuranoside	Sigma-Aldrich	C1768
Cal-520	Abcam	ab171868
Pluronic F-127	Thermo Scientific	P6866
α-Bungarotoxin	Alomone labs	B100
TRIzol	Thermo Scientific	15596026
SYBR Green	Bio Rad	1725270
Triton X-100	Sigma-Aldrich	X100-100ML
SORT-seq reagents	Muraro et al., 2016	N/A
5-CFDA, AM	Thermo Scientific	C1354
Neutral Red Solution	Sigma-Aldrich	N2889
AlamarBlue Cell Viability Reagent	Thermo Scientific	DAL1025
Critical Commercial Assays		
RNeasy Mini Kit	QIAGEN	74104
CellTiter-Glo Luminescent Cell Viability Assay	Promega	G6080
Thermo Scientific reagents for CEL-Seq2	Hashimshony et al., 2016	N/A
Reagents for library preparation from CEL-Seq2	Hashimshony et al., 2016	N/A
Deposited Data		
Raw and analyzed sequencing	This paper	GSE129581
Experimental Models: Cell Lines		
C2C12 Cell Line from mouse	Sigma-Aldrich	91031101
Oligonucleotides		
qPCR_ACTB_F: CTGGCCTAGGACACAGTACG	This paper	N/A
qPCR_ACTB_R: GCTCAGACTCCATTGCAACA	This paper	N/A
qPCR_LGR5_F: GTTCCCCTTCCTGCATGTCT	This paper	N/A
qPCR_LGR5_R: ACCAAACTAGCATCTTTTGCCTT	This paper	N/A
qPCR_ASCL2_F: CACTCGGCTTATTCGTCGGA	This paper	N/A
qPCR_ASCL2_R: CTCCCGAACCAACTGGTGAA	This paper	N/A
qPCR_AXIN2_F: GATAGAAGCTGAGGCAGCCC	This paper	N/A
qPCR_AXIN2_R: CCCCTTCGCATGTCCTCTAC	This paper	N/A
qPCR_RNF43_F: TTCCCATGAGTTCCATCGGC	This paper	N/A
qPCR_RNF43_R: GGCGGTACCTGATGTTGACT	This paper	N/A
qPCR_TCF7L2_F: GCTATCACCGGGCACTGTAG	This paper	N/A
qPCR_TCF7L2_R: GGTCCTCACGAGATTGCCTG	This paper	N/A

(*Continued on next page*)

Continued

REAGENT or RESOURCE	SOURCE	IDENTIFIER
qPCR_MKI67_F: CAGGTGCATGAATCTGGTATTGAA	This paper	N/A
qPCR_MKI67_R: ATTTAGCGCTGCTTCTGTGACC	This paper	N/A
qPCR_3FTX_F: GTGGTGGTGACAATCGTGTG	This paper	N/A
qPCR_3FTX_R: GGTTGCGATGACTGTTGGTT	This paper	N/A
qPCR_KUN_F: GTCCAGGACTCTGTGAACTGC	This paper	N/A
qPCR_KUN_R: GCATTGTTTTGCAGCCAGGTT	This paper	N/A
qPCR_CTL_F: TACACCCCAGGAACCCTTCT	This paper	N/A
qPCR_CTL_R: TATTGGTGACGGAGACGCAC	This paper	N/A
qPCR_HSPA8_F: AGCAGTACAAAGCGGAGGAC	This paper	N/A
qPCR_HSPA8_R: TCTGCCGTGCTCTTCATGTT	This paper	N/A
In situ probe CRISP_F: TGCTGCAACAGTCTTCTGGAAC	This paper	N/A
In situ probe CRISP_R: ATATAGTTTGCATGAAGGGCATCA	This paper	N/A
In situ probe CTL_F: TCTGGGGATTCTGCCTCTTG	This paper	N/A
In situ probe CTL_R: ACTTGCAGATGAAGGGCAGG	This paper	N/A
In situ probe KUN_F: CCCTGCTTAACTTCCCCCAA	This paper	N/A
In situ probe KUN_R: GGCAGGGTCTCCAGGAAGG	This paper	N/A
Software and Algorithms		
AxIS Software	Axion BioSystems	N/A
CFX manager software	Bio-Rad	N/A
Trinity version 2.4.0	Haas et al., 2013	N/A
Read counting	This paper	https://github.com/BuysDB/reptilianOrganoids
Monocle version 2.6.4	Trapnell et al., 2014	N/A
Seurat version 3.0.0.9000	Butler et al., 2018	N/A
RaceID3	Herman et al., 2018	N/A
GraphPad PRISM 7	GraphPad	N/A
LAS X	Leica	N/A
ImageJ	NIH	https://imagej.nih.gov/ij/
Rstudio	Rstudio	Rstudio.com
Adobe illustrator	N/A	N/A
Other		
OrganoPlate	MIMETAS	9603-400-B
MEA-plate	Axion BioSystems	N/A
EVOS Cell Imaging System	Thermo Scientific	N/A
EVOS FL Auto 2 Cell Imaging System	Thermo Scientific	N/A
SP8 or SP8X confocal microscope	Leica	N/A
DM4000 microscope	Leica	N/A

LEAD CONTACT AND MATERIALS AVAILABILITY

Further information and requests for resources and reagents should be directed to the Lead Contact, Hans Clevers (h.clevers@hubrecht.eu).

Unique/stable reagents generated in this study are available and can be requested from the Lead Contact, a completed Materials Transfer Agreement may be required.

EXPERIMENTAL MODEL AND SUBJECT DETAILS

Snakes

All animal procedures complied with local ethical guidelines. Adult *Crotalus atrox* (n = 2) venom glands were purchased from Natural Toxins Research Center in Texas, USA. Adult *Echis ocellatus* (n = 1) and *Deinagkistrodon acutus* (n = 1) venom glands were obtained from snakes maintained at the Liverpool School of Tropical Medicine, UK. Adult *Naja pallida* (n = 1), *Naja nivea* (n = 1) and *Bitis arietans*

(n = 2) venom glands were obtained from residual post-mortem material from Serpo, Rijswijk, the Netherlands. Embryonic *Naja atra* (n = 2), *Naja annulifera* (n = 3) and *Aspidelaps lubricus cowlesi* (n = 7, two different nests) from eggs were obtained from local breeders in the Netherlands. All snakes were captive bred and maintained in individual cages within a temperature, humidity and light-controlled environment according to local protocols for husbandry of venomous snakes. Sex of the animals was not determined as it was presumed to have no biological impact on the experimental procedure or conclusion of the study. Non-invasive venom extraction ('milking') was performed with adult *Echis ocellatus, Deinagkistrodon acutus, Naja pallida*, *Naja nivea* and *Bitis arietans* during lifetime prior to euthanizing and venom gland isolation for organoid culture.

Venom gland organoid cultures

Cells from a single gland were plated in approximately 100 μL Cultrex Pathclear Reduced Growth Factor Basement Membrane Extract (BME) (3533-001, Amsbio). After BME solidification, culture medium was added. Expansion culture medium was based on AdDMEM/F12 (GIBCO) supplemented with B27, Glutamax, HEPES, 100 U/mL Penicillin-Streptomycin (all Thermo-Fisher), 100 mg/mL Primocin (Invivogen), 1.25mM N-acetylcysteine, 10 mM Nicotinamide (both Sigma-Aldrich) and the following growth factors: 2% Noggin conditioned medium (U-Protein Express), 2% Rspo3 conditioned medium (U-Protein Express), 50 ng/mL EGF (Peprotech), 0.5 μM A83-01 (Tocris), 1 μM PGE2 (Tocris), 100 ng/mL FGF10 (Peprotech), 100 nM Gastrin (Tocris). Naja nivea organoid cultures were supplemented with 1 μM FSK (Tocris). For the first seven days after seeding, the expansion medium was supplemented with 10 μM Y-27632 (Abmole). In case of bacterial contaminations following antibiotics were added: 50 mg/mL Gentamicin (Sigma), 2.5 μg/ml Ciprofloxacin (Sigma-Aldrich), 20 μM Erythromycin (Sigma-Aldrich) and 100 nM Azithromycin (Sigma-Aldrich). Ten days after seeding organoids were removed from the BME, mechanically dissociated into small fragments using a Pasteur pipette and re-seeded in fresh BME. Passage was performed in 1:3 – 1:5 split ratio once every ten days for at least 6 months.

C2C12 cell line

The C2C12 mouse myoblast cell line was purchased from Sigma-Aldrich (91031101). Sigma is partnered with the European Collection of Authenticated Cell Cultures (ECACC) repository. Cells were cultured in T75 flasks (734-2705, Corning) in DMEM (11965092, Thermo Fisher Scientific) supplemented with 10% fetal bovine serum (FBS, 16140-071, Thermo Fisher Scientific), 2 mM glutamine (G7513, Sigma-Aldrich) and 1% penicillin/streptomycin (P4333, Sigma-Aldrich) at 37°C. C2C12 cells were routinely tested for mycoplasma contamination and were found negative.

Primary rat cortical neurons

Primary rat cortical cells were isolated from postnatal day 0-1 pups of timed pregnant Wistar rat dams (Envigo) as described previously (Dingemans et al., 2016). Briefly, pups were decapitated and cortices were rapidly dissected on ice and kept in dissection medium (Neurobasal®-A supplemented with 25 g/L sucrose, 450 μM L-glutamine, 30 μM glutamate, 1% penicillin/streptomycin and 10% FBS, pH 7.4) during the entire procedure. Cortices were dissociated to a single-cell suspension by mincing with scissors, trituration and filtering through a 100 μm mesh (EASYstrainer, Greiner). The cell suspension was diluted to a 2 × 106 cells/mL solution. Droplets of 50 μL were placed on the electrode fields in wells of 48-wells MEA plates (Axion BioSystems) pre-coated with 0.1% PEI solution diluted in borate buffer (24 mM sodium borate/50 mM boric acid in Milli-Q, pH adjusted to 8.4). Cells were left to adhere for 2 hours before adding 450 μL dissection medium. Primary rat cortical cultures were kept at 37°C in a humidified 5% CO2 incubator. At day *in vitro* (DIV) 2, 90% of the dissection medium was replaced with glutamate medium (Neurobasal®-A supplemented with 25 g/L sucrose, 450 μM L-glutamine, 30 μM glutamate, 1% penicillin/streptomycin and 2% B27 supplement, pH 7.4) to prevent glial overgrowth. At DIV4, 90% of the glutamate medium was replaced with FBS medium (Neurobasal®-A supplemented with 25 g/L sucrose, 450 μM L-glutamine, 1% penicillin/streptomycin and 10% FBS, pH 7.4).

METHOD DETAILS

Venom gland isolation

In the last week of development (~day 53 – 58), snakes were removed from the egg by an incision in the shell. To avoid bacterial contamination, eggs were briefly rinsed with bleach and 70% ethanol prior to opening in a laminar flow cabinet. Animals were directly euthanized by decapitation. The late-embryonic and adult venom glands were surgically removed and stored on ice in AdDMEM/F12 (GIBCO) supplemented with penicillin/streptomycin.

Venom gland organoid cultures

Isolated venom glands were chopped into small pieces of approximately 1 mm using a scalpel. Muscle and connective tissue were removed and discarded as much as possible. Epithelial tissue pieces were enzymatically digested in 5 mL collagenase (Sigma-Aldrich, C9407, 1 mg/mL) with 10 μM ROCK inhibitor Y-27632 (Abmole, M1817) in AdDMEM/F12 (GIBCO) for about 30 minutes while shaking (120 RPM) at 32°C. The homogeneous cell suspension was pelleted and washed twice with AdDMEM/F12 prior to plating

For differentiation experiments, established organoids were passaged and grown in expansion medium for four days. After four days, the medium was removed and residual medium washed away two times with PBS, after which differentiation medium was added containing; a base of AdDMEM/F12 (GIBCO) supplemented with GlutaMAX, HEPES, 100 U/mL Penicillin-Streptomycin

(all Thermo-Fisher), 100 μg/mL Primocin (InvivoGen), 1.25mM N-acetylcysteine, 10 mM Nicotinamide (both Sigma-Aldrich) and 1 μM PGE2 (Tocris) applied for seven days

Quantification of cell viability/outgrowth efficiency was performed using CellTiter-Glo® accoring to the manufacturer's protocol.

Wnt-conditioned medium was produced as previously described, and used at 50% of the medium volume (Sato et al., 2011).

Images of organoid cultures were taken on EVOS FL Cell Imaging System (Thermo Fisher). Video of beating cilia in organoid was captured (20 frames/second, 20x objective) on EVOS FL Auto 2 (Thermo Fisher).

pLV lentiviral vector containing a CMV promoter driving the expression of TagRFP and Puro resistance gene (via IRES) was transduced in venom gland organoids.

Immunohistochemistry and imaging

Organoids were harvested in cell recovery solution (354253, Corning) and fixed in 4% formaldehyde solution (Sigma-Aldrich) for at least 2 hours at room temperature. Venom glands used for immunohistochemistry (n = 3) were directly embedded in 4% paraformaldehyde upon dissection and fixed for at least 2 hours. Samples were washed and dehydrated by an increasing ethanol gradient before embedding in paraffin. Sections were cut and hydrated before staining. Hematoxylin and eosin (H&E) and periodic acid–Schiff (PAS) staining on organoids and tissue was performed as previously described (Sato et al., 2009). Slides were imaged using a Leica DM4000 microscope.

3D imaging of organoids was performed as described previously (Dekkers et al., 2019). In short, organoids were harvested using ice cold PBS and fixed in 4% paraformaldehyde at 4°C for 45 min. Organoids were then washed with PBT (PBS, 0.1% Tween) and incubated overnight with primary antibodies, B-catenin (H-102, Santa Cruz) and b-tubulin (H-235 Santa Cruz). The next day, organoids were washed with PBT (PBS, 0.1% Tween) and incubated overnight at 4°C with secondary antibodies, Alexa Fluor-647 Phalloidin (both from Thermo Fisher Scientific) and DAPI (Invitrogen). Dense organoids were optically cleared overnight in a glycerol-fructose clearing solution prior to imaging. Cystic organoids were not optically cleared to prevent these from collapsing. Organoid imaging was performed on a Zeiss LSM 880 using a 10x dry and 25x oil immersion objective. Imaris imaging software was used for 3D rendering of images.

For immunofluorescence in the OrganoPlate, cultures were fixed and stained as previously described (Wevers et al., 2018). The following antibodies were used: anti-myosin (A4.1025, DSHB), anti-desmin (ab8470, Abcam), anti-dystrophin (ab15277, Abcam), goat anti-mouse AlexaFluor 555 (A21422, Thermo Fisher Scientific), goat anti-mouse AlexaFluor 647 (A21236, Thermo Fisher Scientific), goat anti-rabbit AlexaFluor 555 (A32732, Thermo Fisher Scientific) and donkey anti-rabbit 647 (SAB4600177, Sigma-Aldrich). The nicotinic acetylcholine receptor was visualized using α-bungarotoxin AlexaFluor 488 (B13422, Thermo Fisher Scientific). Nuclei were stained using Hoechst (H3570, Thermo Fisher Scientific). All steps were performed at room temperature (RT). Cells were imaged using the Micro XLS-C HCl System (Molecular Devices). A 3D reconstruction of a myotube culture was made using Fiji.

In situ *hybridization*

Late embryonic A. l. cowlesi heads (n = 2) were fixed in 4% PFA overnight at 4°C. Fixed heads were divided in two through the midline of the body, separating the left and right venom gland. Material was dehydrated using sequential methanol steps (25, 50, 75, 100%), washed with three times for one hour 100% ethanol and embedded in paraffin. Sections of 10 μm were deparaffinized (nucleoclear, ethanol, Milli-Q) and pretreated (PBST, ProtK 10 min, PBS and 4% PFA). For hybridization, slides were covered with hybridization mix for one hour at 60°C (2% blocking powder, 50% formamide, 5x SSC, 1mg/mL tRNA, 50 μg/mL heparin, 0,1% Triton X-100, 0,1% CHAPS and 5mM EDTA) prior to overnight incubation with probe mix (800 - 1000 ng/mL) at 60°C. On the next day, the slides were washed (2x SSC, 0,1% CHAPS, 50% Formamide) for 30 minutes three times prior to overnight anti-Dig-AP (in 10% sheep serum) incubation at 4°C. Signal was visualized using BM-purple and counterstained with 0,1% neutral red. Images were taken on a Leica DM4000 microscope.

Following primers were used for probe generation:

CRISP F_TGCTGCAACAGTCTTCTGGAAC R_ATATAGTTTGCATGAAGGGCATCA
CTL F_TCTGGGGATTCTGCCTCTTG R_ACTTGCAGATGAAGGGCAGG
KUN F_CCCTGCTTAACTTCCCCCAA R_GGCAGGGTCTCCAGGAAGG

Electron microscopic analysis

Aspidelaps lubricus organoid lines (n = 2 organoid lines derived from different individuals) were harvested in cell recovery solution (354253, Corning) to remove BME and fixed by chemical fixation using 3% glutaraldehyde in cacodylate buffer. The fixation was followed by 1% osmium tetroxide plus 1.5% potassium ferrocyanide postfixation. Then, the organoids were dehydrated in series of ethanol and gradually embedded in Epon resin. Ultrathin sections were observed in a Tecnai Spirit T12 Electron Microscope equipped with an Eagle CCD camera (Thermo Fisher Scientific).

Organoid protein extraction

Aspidelaps lubricus organoids were grown and differentiated as described above. For LC-MS analysis, a minimum of 500 μL of organoid containing BME (~25 droplets) was harvested for protein extraction. In short, differentiation medium was removed and

any residual liquid removed with PBS washes, organoids were collected and mechanically dissociated in 500 μL PBS using a glass Pasteur pipette in a 1.5 mL eppendorf tube. Tubes were sonicated for 15 cycles (30 s on, 30 s off) using the Bioruptor Plus (Diagnode). Any leftover debris was spun down at 12,000 rpm, the supernatant collected, snap frozen on dry ice and stored at −80°C.

For functional toxicity readout, a minimum of 500 μL of organoid containing BME was washed in the tissue culture plate with PBS and supplemented with C2C12 differentiation medium for two days prior to collection of supernatants. The same procedure was applied to harvest supernatant from human colon control organoid cultures as a negative control (Sato et al., 2011).

Liquid chromatography–mass spectrometry and Mascot database search

For comparison of *A. l. cowlesi* crude venom and organoid extracts, liquid chromatographic separation was performed with parallel at-line nanofractionation and mass spectrometry analysis. MS data of venom and organoid samples was analyzed for identical masses found in the samples to confirm production of venom toxins by organoids.

LC separation was performed using a Shimadzu UPLC system ('s Hertogenbosch, the Netherlands), and a 250 × 4.6 mm Waters Xbridge Peptide BEH300 C18 analytical column with a 3,5-μm particle size combined with a 300-Å pore size. Separations were performed in a Shimadzu CTD-30A column oven at 30°C. Mobile phase A comprised of 98% H2O, 2% ACN and 0.1% FA, and mobile phase B comprised of 98% ACN, 2% H2O and 0.1% FA. A linear increase of mobile phase B from 0% to 50% in 20 min was followed by a linear increase from 50% to 90% B in 4 min and a 5 min isocratic separation at 90% B. The starting conditions were reached again in 1 min and the column was then equilibrated for 10 min at 0% B. A post-column flow split in 1:9 ratio directed the larger fraction to a FractioMateTM FRM100 nanofraction collector (SPARK-Holland & VU, Netherlands, Emmen & Amsterdam) or a modified Gilson 235P autosampler. To further confirm that venom toxins were present in the organoid extracts, crude organoid extracts were subjected to tryptic digestion after which these were analyzed with nanoLC-MS/MS. For this, 20 μL of each organoid sample was transferred to an Eppendorf tube containing 15 μl of digestion buffer (25 mM NH4HCO3, pH 8.2). Subsequently, 1.5 μl of reducing agent (0.5% β-mercaptoethanol) was added to each tube followed by a 10-min incubation step at 95°C. Post incubation, the samples were cooled to room temperature and centrifuged at 150 RCF for 10 s in a Himac CT 15RE centrifuge. Next, 3 μL of alkylating agent (55 mM iodoacetamide) was added to the tubes before incubation in the dark at room temperature for 30 min. Next, 3 μL of 0.1 μg/μL trypsin was added before incubation at 37°C for 3 h, and then an additional 3 μl of trypsin was added to the tubes and the samples were incubated overnight. Subsequently, 1 μL of 5% FA was added to quench the digestion, followed by brief centrifugation to remove any particulate matter. Finally, the samples were centrifuged for 10 s at 150 RCF and the supernatants were transferred to autosampler vials with glass inserts and analyzed with nanoLC-MS/MS. The data files obtained were run through the Mascot search engine (MASCOT; Matrix Science, London, United Kingdom) against the Swiss-Prot, NCBInr database.

Myotube cultures

C2C12 cells were harvested and resuspended to obtain a cell suspension of 5,000 cells/μL in cold medium supplemented with 1:25 Matrigel-GFR (356231, Corning). The C2C12 cell suspension was seeded in the perfusion channel of an OrganoPlate 2-lane (9603-400B, Mimetas) against a collagen-I ECM gel as previously described (Wevers et al., 2018). The plate was incubated on a flat surface for 3 hours to allow cell attachment, after which medium perfusion was started with C2C12 differentiation medium composed of DMEM supplemented with 2% horse serum (26050-088, Thermo Fisher Scientific), 1 μM insulin (I9278, Sigma-Aldrich), 2 mM glutamine, and 1% penicillin/streptomycin. From day 2-5, the differentiation medium was supplemented with 10 μM cytarabine (C1768, Sigma-Aldrich) to inhibit cell proliferation.

For cell viability assay, C2C12 cells were exposed for 30 minutes to supernatant from *Aspidelaps lubricus* venom gland organoids, supernatant from human colon organoids, recombinant alpha bungarotoxin and a killing control. After that exposure was terminated and fresh medium added for 24h and 48h. WST8 assay was used according to the manufacturer's protocol to quantify cell viability.

Calcium imaging

Calcium imaging assays were performed at day 8 after plating. C2C12 myotubes in the OrganoPlate were incubated with 20 μM Cal-520 (ab171868, Abcam), 0.04% Pluronic-127 (P6866, Thermo Fisher Scientific) in C2C12 differentiation medium without serum for 60 minutes at 37°C, followed by 30 more minutes at RT. Next, cultures were exposed to C2C12 differentiation medium (negative control), human colon organoid supernatant (negative control), snake venom gland organoid supernatant or 10 μM α-bungarotoxin (positive control) for 30 minutes. Calcium imaging recordings were made using an ImageXpress Micro XLS-C Confocal High-Content Imaging System (Molecular Devices, wide field mode, 4x magnification, 2 Hz). An individual chip was imaged for 90 s to record baseline calcium activity. Myotubes in the chip were then exposed to 500 μM carbachol or vehicle (0.5% water) and immediately placed back in the microscope for another 90 s of calcium imaging to record the response to carbachol or vehicle. This pipeline was repeated for each chip.

The calcium imaging recordings were processed using scripts developed in Fiji (Schindelin et al., 2012). Recordings were corrected for camera-induced noise via Kalman Filtering and corrected for bleaching. Movement of fluorescent signal was quantified via Gaussian Window MSE resulting in RGB-encoded videos showing movement of fluorescent signal to the left and right side in purple and green, respectively. The colored areas were measured per time frame and averaged over time. All videos were processed to correct for flow-induced artifacts caused by movement of fluorescent cell debris. In the case of calcium wave propagation, movement was detected to a similar extent in both the left and right direction (< 2 fold difference) and the average area of the two directions

was determined. In the case of flow of fluorescent debris, the movement detected in one direction is dominant over the other (> = 2 fold difference) and movement in the dominant direction was excluded.

MEA recordings rat cortical neurons

Spontaneous electrical activity was recorded on the day of exposure (DIV9-11) as described previously (Nicolas et al., 2014; Tukker et al., 2018). In short, signals were recorded using a Maestro 768-channel amplifier with integrated heating system and temperature controller and a data acquisition interface (Axion BioSystems). Data acquisition was managed with Axion's Integrated Studio (AxIS 2.4.2.13) and recorded as. RAW files. All channels were sampled at the same time with a gain of 1200x and a sampling frequency of 12.5kHz/channel with a 200-500 Hz band-pass filter. Prior to the recording, MEA plates were allowed to equilibrate for ~10 min in the Maestro.

Spontaneous neuronal activity was recorded prior to exposure to generate a baseline recording. Immediately following this recording, cells were exposed to the test compounds (α-bungarotoxin, organoid supernatant and vehicle control) and activity was recorded for another 30 min. Each well was exposed to only one single concentration of one compound in order to prevent receptor (de)sensitization.

To determine (modulation of) spontaneous activity,. RAW data files were re-recorded to obtain Alpha Map files. In this re-recording, spikes were detected with the AxIS spike detector (Adaptive threshold crossing, Ada BandFlt v2) and a variable threshold spike detector set at 7x standard deviation (SD) of internal noise level (rms) on each electrode. Post/pre-spike duration was set to 3.6/2.4 ms respectively. For further data analysis, spike files were loaded in NeuralMetric Tool (version 2.2.4, Axion BioSystems) and only active electrodes (MSR ≥ 0.1 spikes/s) in active wells (≥1 active electrode) were included in data analysis. The effects of test compounds on spontaneous activity were determined by comparing the baseline activity with activity following exposure. A custom-made MS Excel macro was used to calculate treatment ratios (TR) per well for the mean spike rate, which were normalized to appropriate vehicle control.

For cell viability, rat cortical cells were cultured at a density of 3.0 × 104 cells/well. At DIV9-10, cells were exposed for 24 h to the test compounds, after which cell viability was assessed using a combined CFDA-AM / neutral red / alamar blue assay. In short, cells were incubated for 30 minutes with 12.5 mM alamar blue and 4 mM CFDA-AM in FBS at 37°C. Resorufin was measured spectrophotometrically at 540/590 nm (Infinite M200 microplate; Tecan), whereas hydrolyzed CFDA was measured spectrophotometrically at 493/541 nm. The aB/CFDA solution was then replaced by 200 mL neutral red solution (175 mM in PBS, Invitrogen) for 1 h at 37°C. Next, cells were incubated for 30 min with 200 mL extraction solution (1% glacial acetic acid, 50% ethanol, and 49% H2O) during gentle shaking at room temperature. After 30 min extraction, fluorescence was measured spectrophotometrically at 530/645 nm.

RNA extraction and de-novo transcriptome assembly

RNA isolations of organoids and tissues for *de-novo* transcriptome assembly and bulk RNA sequencing were performed using TRIzol (Invitrogen) following the manufacturer's instructions. Organoid RNA isolations for quantitative PCR were performed with RNeasy Mini Kit (QIAGEN) following the manufacturer's instructions. Quantitative PCR analysis was performed using the SYBR Green and Bio-Rad systems. Changes in expression were calculated using CFX manager software (Bio-Rad). Primers were designed using NCBI primer design tool with the coding sequence of annotated scaffolds of interest as input. Primers used in this study are;

ACTB, F_CTGGCCTAGGACACAGTACG,R_GCTCAGACTCCATTGCAACA
LGR5,F_GTTCCCCTTCCTGCATGTCT,R_ACCAAACTAGCATCTTTTGCCTT
ASCL2,F_CACTCGGCTTATTCGTCGGA,R_CTCCCGAACCAACTGGTGAA
AXIN2,F_GATAGAAGCTGAGGCAGCCC,R_CCCCTTCGCATGTCCTCTAC
RNF43,F_TTCCCATGAGTTCCATCGGC,R_GGCGGTACCTGATGTTGACT
TCF7L2,F_GCTATCACCGGGCACTGTAG,R_GGTCCTCACGAGATTGCCTG
MKI67,F_CAGGTGCATGAATCTGGTATTGAA,R_ATTTAGCGCTGCTTCTGTGACC
*3FTX,F*_GTGGTGGTGACAATCGTGTG,R_GGTTGCGATGACTGTTGGTT
KUN,F_GTCCAGGACTCTGTGAACTGC,R_GCATTGTTTTGCAGCCAGGTT
CTL,F_TACACCCCAGGAACCCTTCT,R_TATTGGTGACGGAGACGCAC
HSPA8,F_AGCAGTACAAAGCGGAGGAC,R_TCTGCCGTGCTCTTCATGTT

Sequencing and de-novo transcriptome assembly was performed by BaseClear B.V. as follows: PolyA enriched RNA from liver tissue, pancreas tissue, venom gland tissue, organoids early passage, organoids late passage expansion and organoids late passage differentiation was sequenced. Paired-end sequence reads were generated using the Illumina HiSeq2500 system. FASTQ sequence files were generated using bcl2fastq2 version 2.18. Initial quality assessment was based on data passing the Illumina Chastity filtering. Subsequently, reads containing PhiX control signal were removed using an in-house filtering protocol. The second quality assessment was based on the remaining reads using the FASTQC quality control tool version 0.11.5. The transcriptome assembly was performed with Trinity (version 2.4.0) (Haas et al., 2013), using the combined data of all six samples. The resulting consensus assembly was filtered to remove all sequences shorter than 500bp, resulting in 311,948 remaining scaffolds. These

were aligned with BLASTN (version 2.6.0) against a local copy of the NCBI-NT database (built in February 2018). Toxin-encoding contigs were validated by manual sequence analysis (e.g., ORF identification) of those exhibiting annotations consistent with known snake venom toxin proteins.

Bulk and single cell RNA sequencing

Bulk RNA sequencing of *N. nivea* was performed by the Utrecht Sequencing Facility (uSeq) as follows: Libraries were prepared based on polyA enrichment. Paired-end sequence reads were generated using the NextSeq500 system.

For organoid single cell RNA sequencing, *A. l. cowlesi* organoids were grown and differentiated as described above. BME was removed by washing in ice-cold DMEM (GIBCO). For tissue sequencing, embryonic *A. l. cowlesi* venom glands were dissociated with collagenase I as described above and subsequently processed in the same way as organoids. Organoids or tissue fragments were resuspended in TrypLE Express (GIBCO) pre-heated to 32°C and dissociated under repeated pipetting. Upon reaching single cell state, samples were pelleted, washed, resuspended in FACS buffer (advanced DMEM, 10 mM Y-27632 and DAPI) and strained (35 μm). Cells were immediately sorted into 384-well plates containing ERCC spike-ins (Agilent), RT primers and dNTP (Promega) using a BD FACSJazz (BD Biosciences). Plates were prepared using Mosquito HTS (TTPlabtech). scRNA-seq libraries were prepared following the SORT-seq protocol (Muraro et al., 2016), which is based on the CEL-seq2 method (Hashimshony et al., 2016). Briefly, cells were first lysed for 5 min at 65 °C, and RT and second-strand mixes were dispensed by the Nanodrop II liquid handling platform (GC Biotech). Single-cell double-stranded cDNAs were pooled together and *in vitro* transcribed for linear amplification. Illumina sequencing libraries were prepared using the TruSeq small RNA primers (Illumina) and these DNA libraries were sequenced paired-end at 60 and 26 bp read length, respectively, on the Illumina NextSeq.

Bulk and single cell RNA sequencing analysis

Bulk paired-end reads of *A. l. cowlesi* and *N. nivea* tissue and organoids were mapped to the *de novo* assembled *A. l. cowlesi* transcriptome using STAR. When a read mapped to multiple scaffolds, a fractional count of 1/x was recorded, where x is the number of scaffolds the read maps to. To reduce the complexity of the count table, scaffolds with identical blast hits were merged by summation of their transcript counts. All scripts used for read counting are deposited at https://github.com/BuysDB/reptilianOrganoids. For single cell analysis, paired-end reads were demultiplexed on the cell barcode and UMI and adapters trimmed using Cutadapt 2. Next, the reads were mapped and counted as described for the bulk samples, additionally we removed amplification duplicates by UMI-scaffold combinations. Scaffold annotations were filtered to exclude the terms (“mitochondrial,” “mitochondrion,” “ribosomal,” “rRNA,” “ribosomal,” “microsatellite,” “transposon,” “SINE,” “LINE repeat,” “noBlast”) and requiring them to be detected in at least 2 cells, resulting in 42,507 unique annotations. Subsequently, cells were filtered by requiring at least 2000 counts and at least 100 different genes to be expressed, leaving 1,092 cells (1,255 for tissue) to be included for dimensionality reduction and k-medoids-based clustering using RaceID3 according to the vignette (Herman et al., 2018), starting with an expected cluster number of 10 (organoid) and 20 (tissue). Violin plots were generated using Seurat functions (Butler et al., 2018) (version 3.0.0.9000) on the dataset analyzed by RaceID3. Single cell trajectories were analyzed using Monocle (version 2.6.4) (Trapnell et al., 2014). In short, genes were selected as input features based on differential expression between expansion and differentiation medium and dimensionality was reduced for display using reverse graph embedding.

QUANTIFICATION AND STATISTICAL ANALYSIS

No statistical methods were used to predetermine sample size. The experiments were not randomized and the investigators were not blinded to the sample allocation during experiments and outcome assessment. All data are presented as mean ± standard error of the mean (SEM), unless stated otherwise. Value of n is always displayed in the figure as individual data points, more information can be found in the figure legends. Statistical tests included unpaired two-tailed t test for Figures 1D, S1C, S6I, and S7E–S7G and paired two-tailed t test for Figures S7B–S7D using GraphPad Prism. ns $p > 0.05$, * $p \leq 0.05$, ** $p \leq 0.01$, *** $p \leq 0.001$, **** $p \leq 0.0001$.

DATA AND CODE AVAILABILITY

All bulk and single cell RNA sequencing data of this study have been deposited in the Gene Expression Omnibus (GEO) under accession code GSE129581.

Supplemental Figures

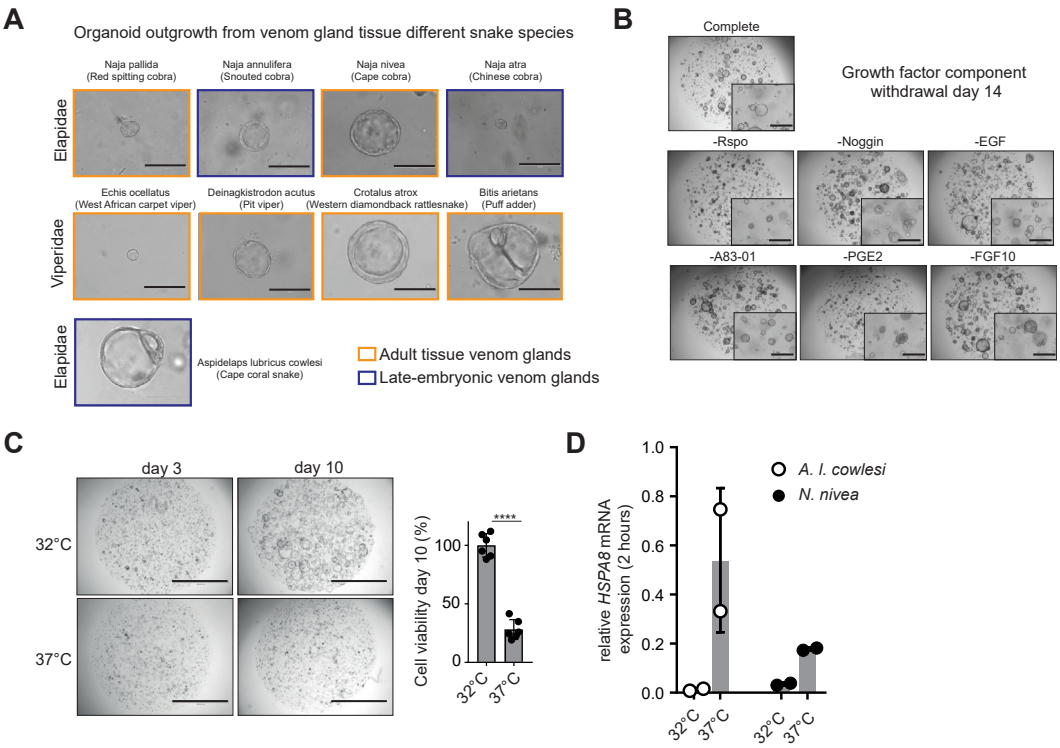

G

Name	Toxin class
Oxyuranus scutellatus scutellatus toxin 3 mRNA, complete cds	3FTX
Naja sputatrix post synaptic alpha neurotoxin precursor (ntx) gene, ntx-4 allele	3FTX
Pseudechis rossignolii Pr-SNTX mRNA for three-finger toxin, complete cds	3FTX
Naja atra gene encoding cardiotoxin 4	3FTX
Laticauda laticaudata LIL gene for long chain neurotoxin, partial cds	3FTX
Ophiophagus hannah isolate OH-35 short chain alpha neurotoxin precursor	3FTX
Laticauda semifasciata (sea snake) gene for erabutoxin c	3FTX
Bungarus flaviceps muscarinic toxin-like protein mRNA, complete cds	3FTX
Naja atra clone n031_7f_1 three-finger toxin precursor, gene, partial cds	3FTX
Bungarus flaviceps non-conventional three finger toxin isoform 6 mRNA	3FTX
Pseudechis rossignolii Pr-LNTX mRNA for three-finger toxin, complete cds	3FTX
Naja kaouthia kaouthin-2 precursor, mRNA, complete cds	CRISP
Ophiophagus hannah opharin precursor, mRNA, complete cds	CRISP
Laticauda semifasciata latisemin mRNA, complete cds	CRISP
Bungarus multicinctus clone B218_4L_2 three-finger toxin precursor, genes,	Kunitz
Austrelaps labialis putative Kunitz-type proteinase inhibitor mRNA	Kunitz
Naja atra aci gene for chymotrypsin inhibitor precursor, exons 1-3	Kunitz
Naja atra mRNA for chymotrypsin inhibitor (aci gene)	Kunitz
Bungarus fasciatus L-amino acid oxidase mRNA, complete cds	LAAO
Macropisthodon rudis isolate PDE-1 phosphodiesterase gene, partial cds	PDE
Naja atra K-like metalloprotease precursor, mRNA, partial cds	SVMP
Naja naja cobrin precursor, mRNA, complete cds	SVMP
Naja atra metalloproteinase atrase A mRNA, complete cds	SVMP
Naja atra metalloproteinase atrase B mRNA, complete cds	SVMP
Drysdalia coronoides MTP4 mRNA, complete cds	SVMP
Naja atra atragin precursor, mRNA, partial cds	SVMP
Micrurus corallinus MCOR0067C C-type lectin precursor, mRNA	CTL
Demansia vestigiata vestiginin-2 precursor, mRNA, complete cds	Waprin

(legend on next page)

Figure S1. Culture Characteristics and Toxins of Venom Gland Organoids in Mammalian Growth Factor Medium, Related to Figures 1 and 2

(A) Organoid outgrowth from venom gland tissue of different Elapidae (n = 5) and Viperidae (n = 4) snake species. Origin of tissue was from either adult venom glands (orange) or late embryonic venom glands (blue). Scale bars, 200 μm.

(B) Representative images of organoid outgrowth in complete medium or medium without one of the indicated components for 14 days. This dropout screen was performed on established organoids (passage 3). Scale bars, 400 μm.

(C) Brightfield images and quantification of *A. l. cowlesi* organoids grown in complete expansion medium at 32°C or 37°C from the moment of splitting into a near single cell suspension to day 3 and day 10 after plating. Viability determined at day 10 using CellTiter-Glo, normalized to cells at 32°C. Scale bars, 2000 μm. Data points represent technical replicates. **** = $p \leq 0.0001$.

(D) Relative *HSPA8* expression normalized to *ACTB* determined by qPCR. For *A. l. cowlesi* and *N. nivea* organoids at 32°C and 37°C for 2 hours. Data points represent biological replicates.

(E) Images of successful lentiviral transduction of venom gland organoids. Detection of histone 2B-RFP (H2B-RFP) stable construct integration and nuclear expression in red. Scale bars, 200 μm.

(F) Transmission electron microscopy image of ciliated cell present in *A. l. cowlesi* organoid. Scale bar, 5 μm.

(G) Highest expressed toxin genes in *A. l. cowlesi* venom gland organoids. Table of *de novo* scaffold BLASTN hit and toxin class.

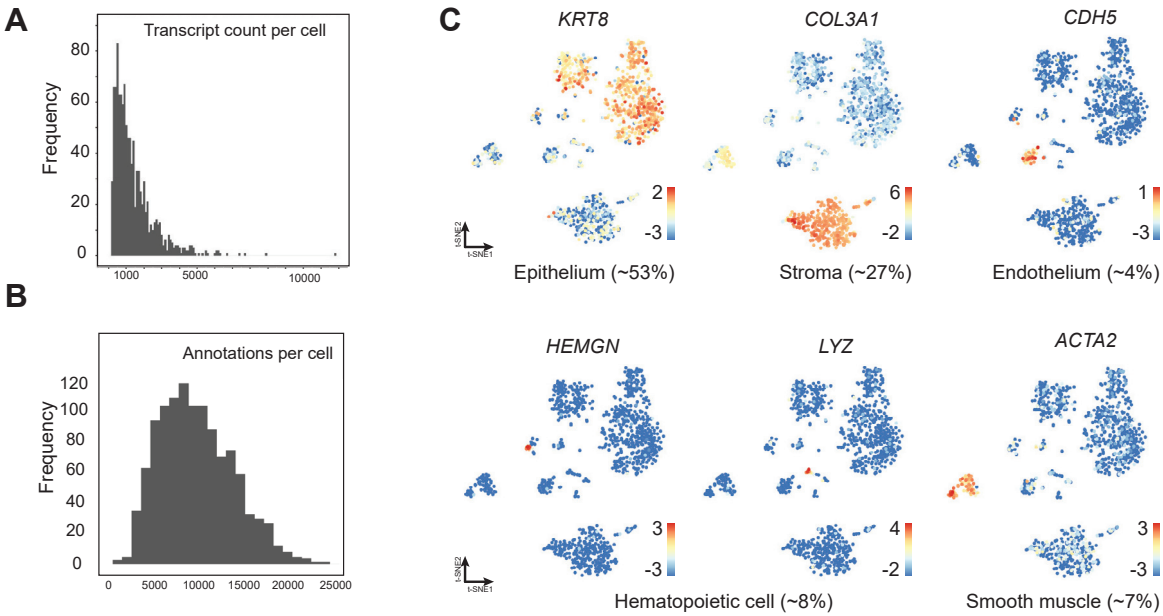

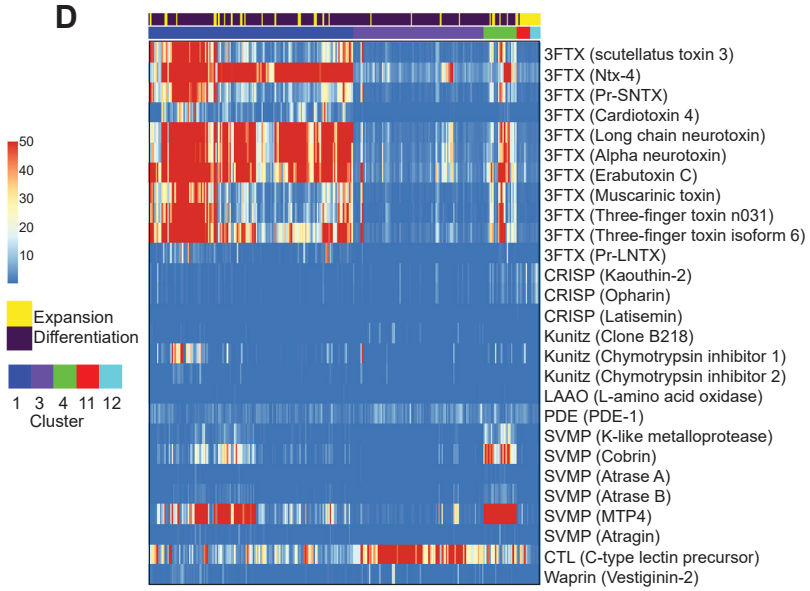

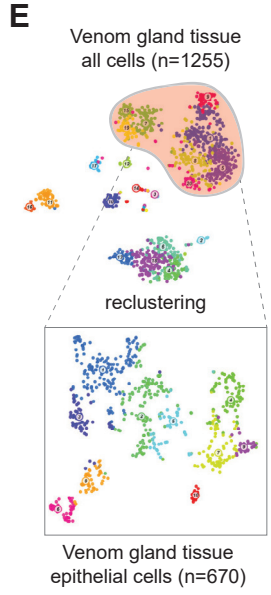

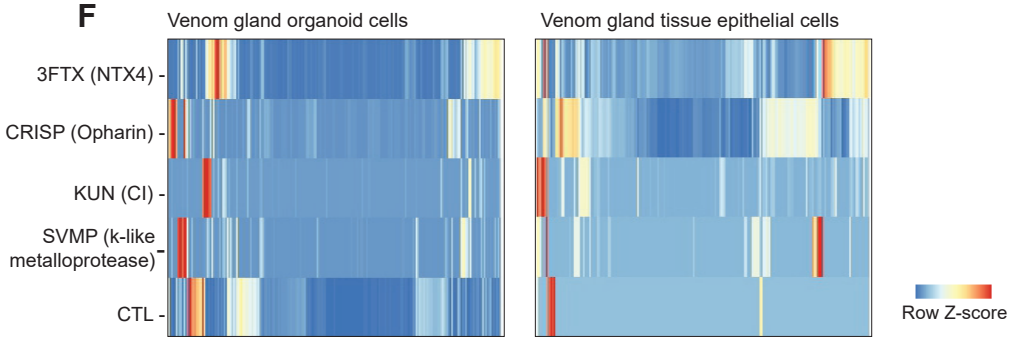

(legend on next page)

Figure S2. Single-Cell Transcriptome Analysis of Venom Gland Primary Tissue and Organoid Cells, Related to Figure 4

(A) Details on single cell sequencing analysis; transcript count per cell.

(B) Details on single cell sequencing analysis; annotations per cell.

(C) Single cell RNA sequencing: clustering of *A. l. cowlesi* primary venom gland tissue cells (n = 1255) visualized by *t*-distributed stochastic neighbor-embedding (*t*-SNE) map. Expression level of cell type marker genes in *t*-SNE map (color coded logarithmic scale of transcript expression): epithelial cells, *KRT8* (n = 670); stromal cells, *COL3A1* (n = 342); hematopoietic cells, *HEMGN*, *LYZ* (n = 103); smooth muscle cells, *ACTA2* (n = 90); endothelial cells, *CDH5* (n = 50).

(D) Heatmap of toxin gene (y axis) expression per individual cell (x axis). All cells from toxin-expressing clusters 1, 3, 4, 11 and 12 are displayed for expression of most abundant toxin genes, see Figure S2B. Color coded expansion medium, differentiation medium and cluster numbers.

(E) Schematic representation of reclustering epithelial cells (10 clusters, n = 670) from total venom gland tissue dataset (20 clusters, n = 1255). Visualized by *t*-distributed stochastic neighbor-embedding (*t*-SNE) map.

(F) Heatmap of expression per toxin class (3FTx, CRISP, KUN, SVMP and CTL) of highest expressed genes (*NTX4, Opharin, Chymotrypsin inhibitor, K-like metalloprotease* and *CTL*) (y axis) per cell (x axis) for both organoids and epithelial tissue cells.

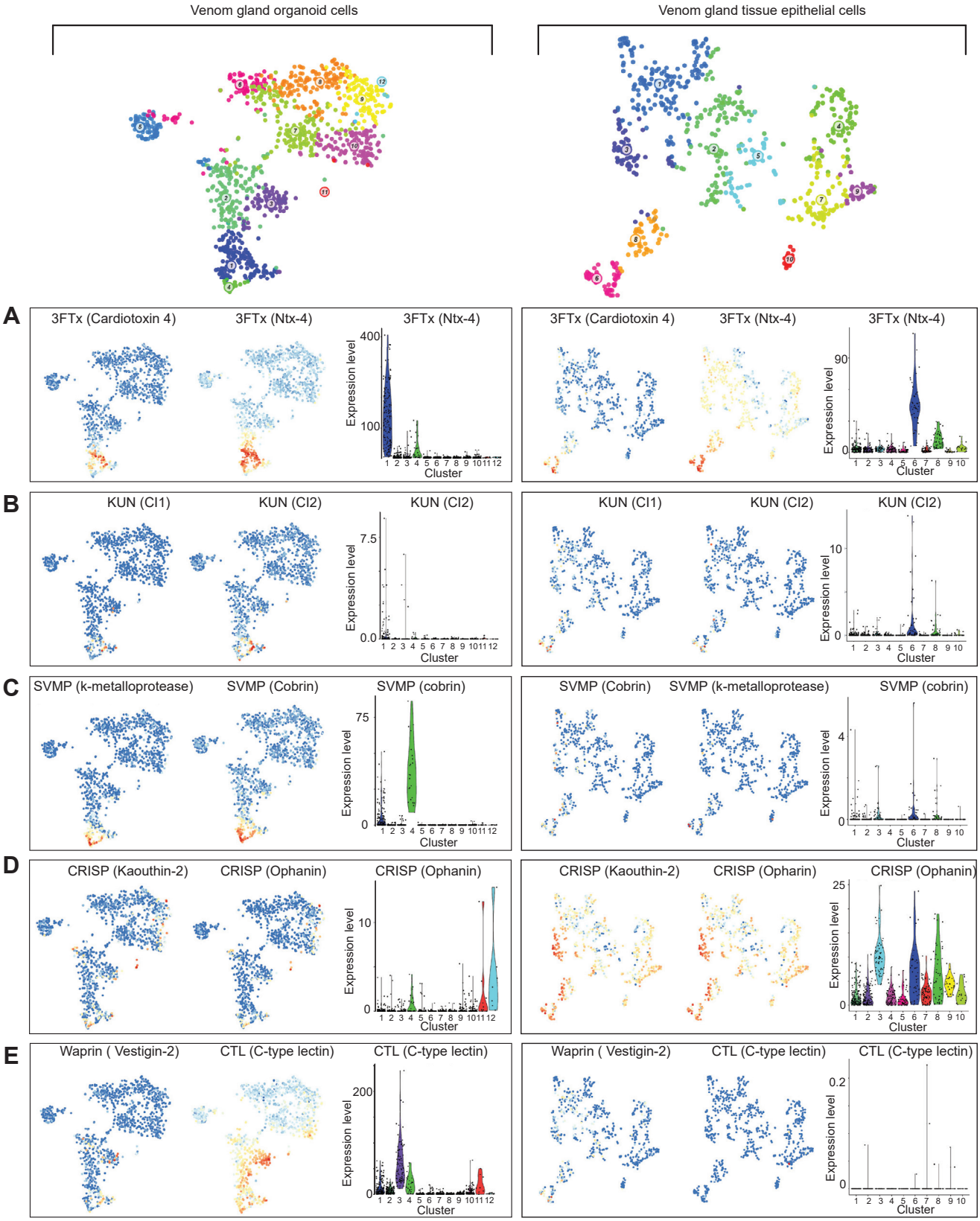

(legend on next page)

Figure S3. Dedicated Venom Gland Epithelial Cells Express Different Classes of Toxins, Related to Figure 4

(A–E) Expression levels of selected toxin genes in *t*-SNE map (color coded logarithmic scale of transcript expression) and violin plots visualizing expression levels of cluster-enriched toxins. Left panels are venom gland organoid cells and right panels are venom gland tissue epithelial cells, both from *A. l. cowlesi*.

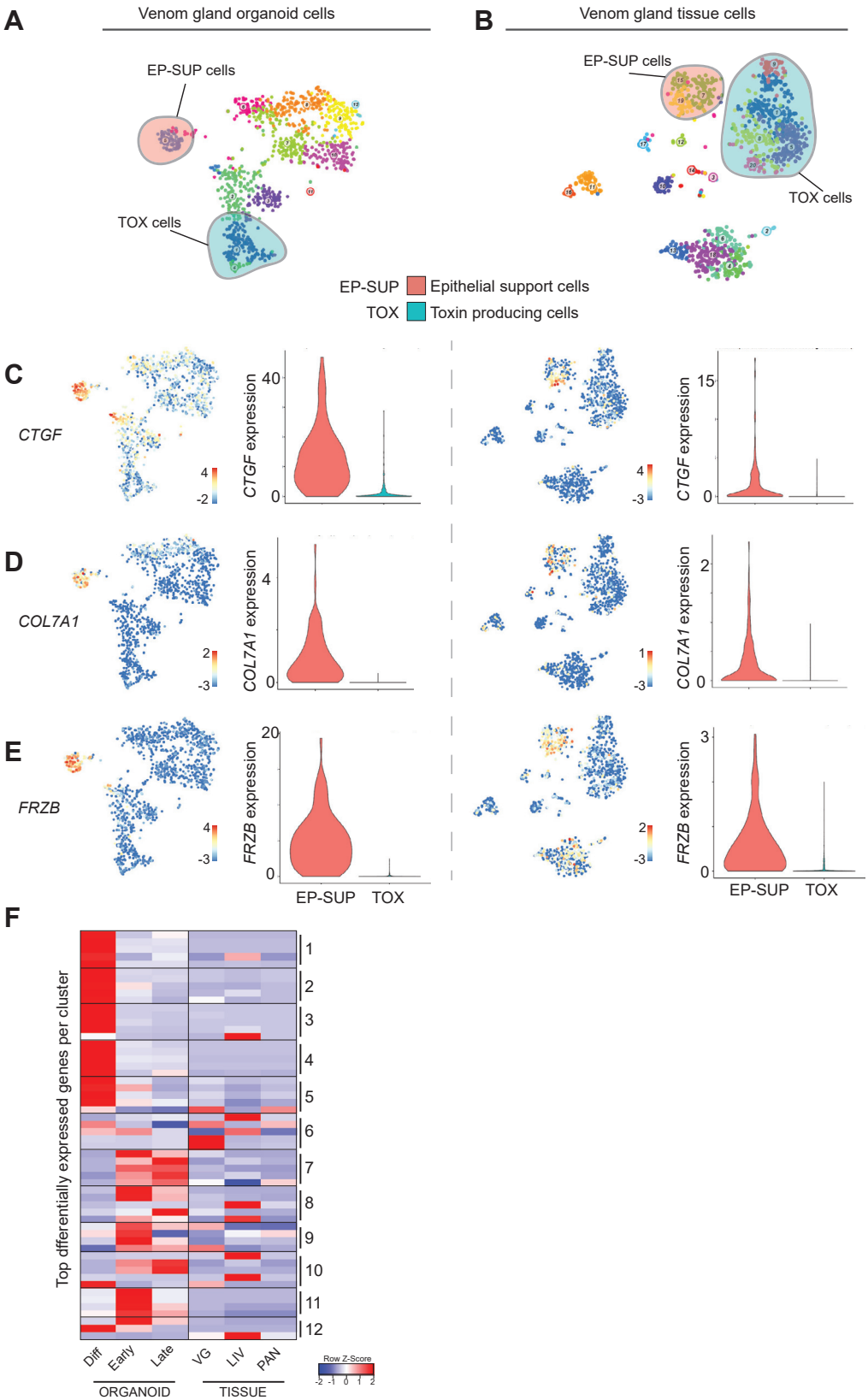

(legend on next page)

Figure S4. Two Different Lineages of Epithelial Cells Captured in Organoids and Primary Tissue, Related to Figure 4

(A) *t*-SNE map of organoid dataset, highlighted are the clusters that account for the EP-SUP and TOX lineage.

(B) *t*-SNE map of tissue dataset, highlighted are the clusters that account for the EP-SUP and TOX lineage.

(C–E) Expression levels of selected EP-SUP genes in *t*-SNE map (color coded logarithmic scale of transcript expression) and violin plots visualizing expression levels in the two distinct lineages. Left panels are organoid cells and right panels are tissue cells.

(F) Heatmap of marker expression (12 clusters (3 to 5 genes per cluster) from organoid single cell sequencing dataset (Figure 4) in bulk mRNA samples from venom gland organoids in differentiation (Diff) and expansion medium early (Early) and late (Late) and venom gland (VG), liver (LIV) and pancreas (PAN) tissue. Expression levels visualized as color coded Row Z-score.

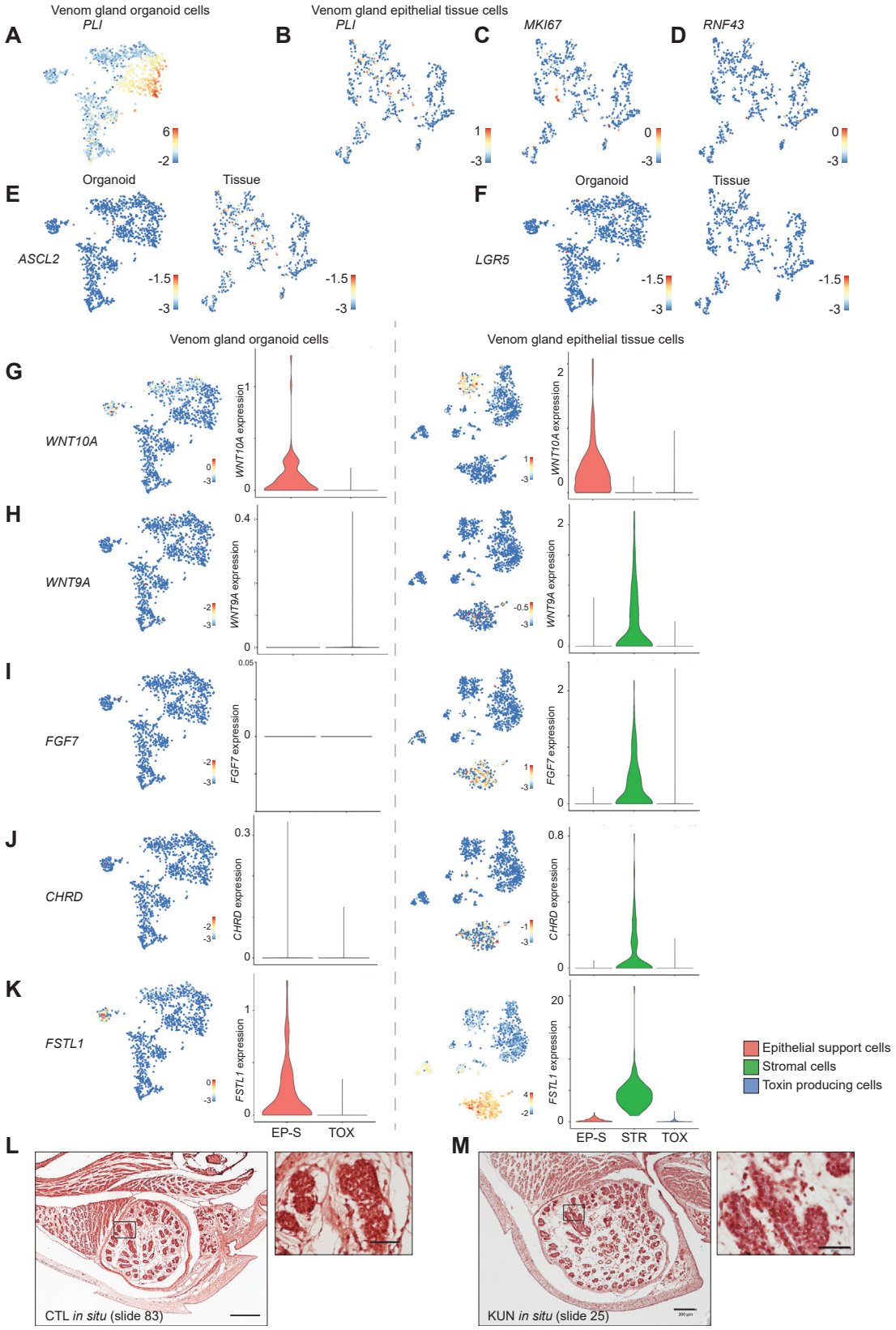

(legend on next page)

Figure S5. Non-venomous Cells Express Stem Cell Markers and Niche Factors, Regional Heterogeneity in CTL, and KUN Expression *In Vivo*, Related to Figures 4, 5, and 6

(A–F) Expression levels of selected genes in *t*-SNE map (color coded logarithmic scale of transcript expression). Left panels are organoid cells and right panels are tissue cells.

(G–K) Expression levels of selected niche signal genes in *t*-SNE map (color coded logarithmic scale of transcript expression) and violin plots visualizing expression levels in the distinct lineages. Left panels are organoid cells and right panels are tissue cells.

(L–M) Representative images of venom gland proximal and distal sections. BM-purple stain of *in situ* hybridization. Lack of detectable CTL (slide 83, distal) and KUN (slide 25, proximal) signal in *A. l. cowlesi* venom gland tissue. Scale bars, 200 μm, close up panels 50 μm.

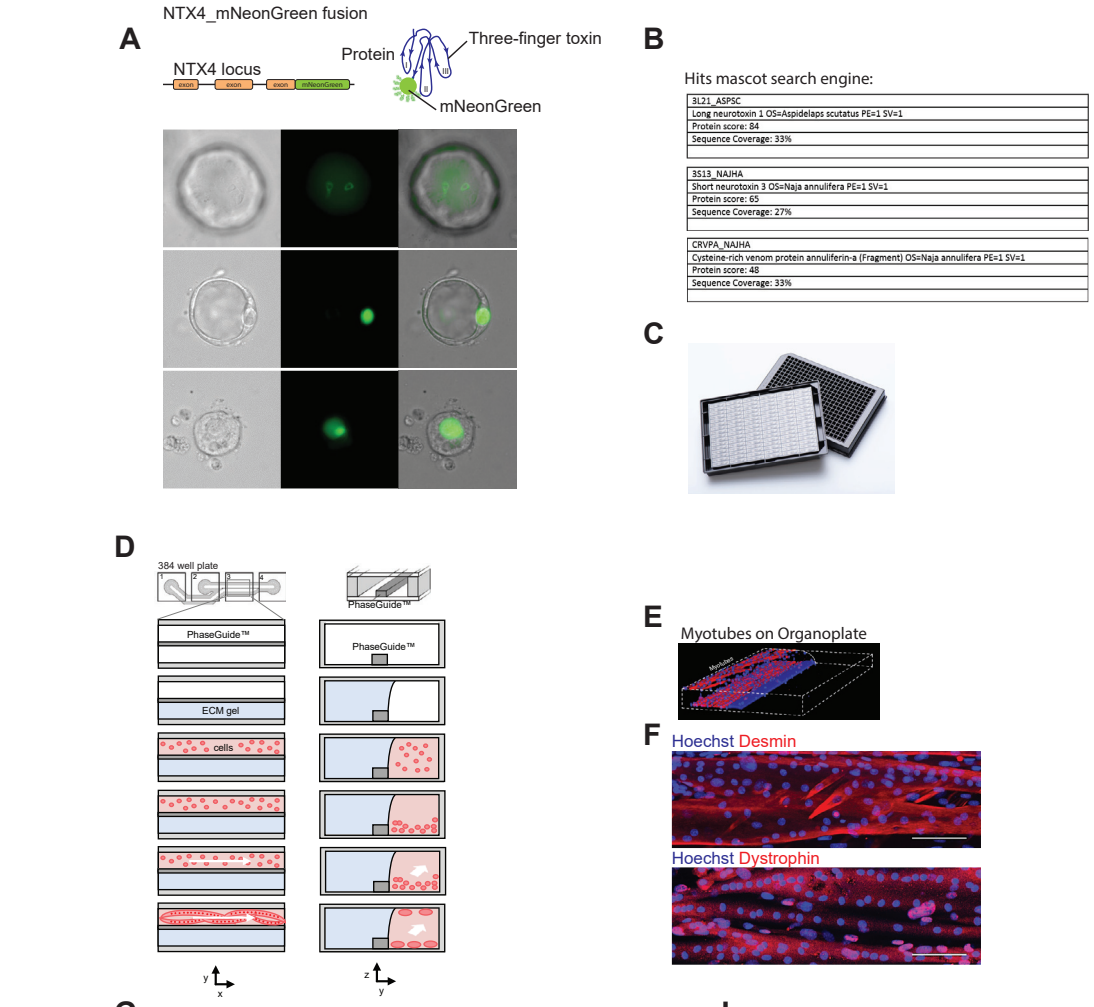

(legend on next page)

Figure S6. Venom Gland Organoids Functionally Secrete Proteins that Block Calcium Signals in Muscle Cells on OrganoPlate, Related to Figure 7

(A) Example of protein hits obtained with a Mascot search of the spectra measured from LC-MS analysis. Based on tryptic digest of an organoid supernatant.
(B) Generation of an endogenous fluorescent tag of three-finger toxin *NTX4* using CRISPR-HOT in *A. l. cowlesi* organoids
(C) MIMETAS 2-lane OrganoPlate
(D) Schematic overview of OrganoPlate microfluidic network covering four wells of the 384-well-plate.
(E) Representative immunofluorescent 3D reconstruction of myotubes forming a perfusable tube structure. Staining for Hoechst (blue) and Myosin (red).
(F) Confocal image of mature myotubes stained for Desmin, Dystrophin (red) and Hoechst (blue).
(G) Cultures were exposed to different supernatants in chips, after which calcium wave propagation was imaged before and after carbachol stimulation. Maximum projected images depict calcium wave propagation over all image frames after carbachol exposure, in which purple reflects activity to the left and green to the right.
(H) Quantification of (F). The total calcium wave movement was calculated before and after carbachol stimulation based on total fluorescent signal. Data points represent biological replicates.
(I) Cell viability assay (WST8) of C2C12 murine muscle cultures 24h and 48h after a 30-minute exposure to supernatants. Data points represent biological replicates. ns = not significant.

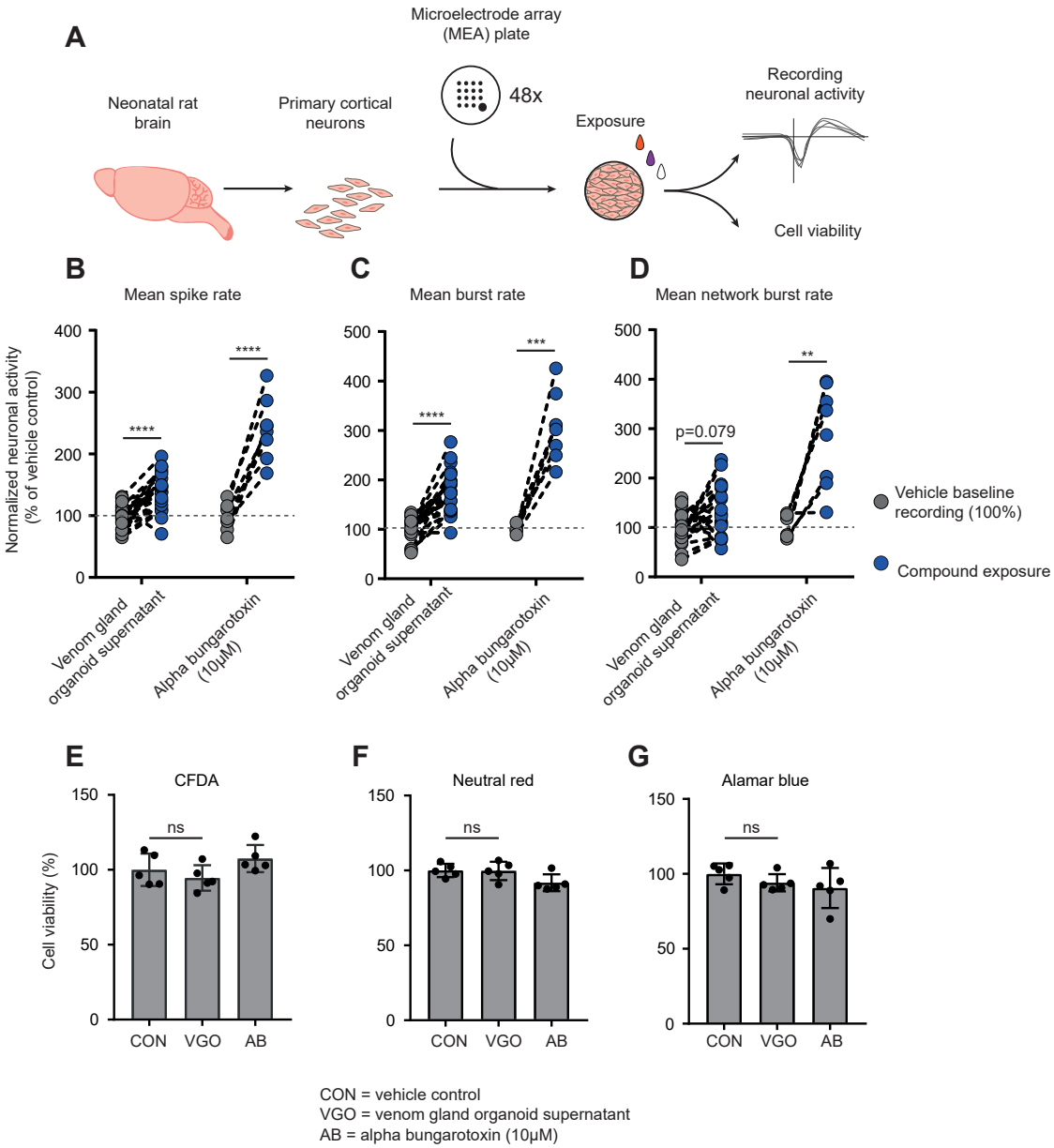

Figure S7. Venom Gland Organoid Proteins Increase Neuronal Activity in Rat Cortical Neurons, Related to Figure 7

(A) Schematic representation of experimental setup. Culture of neonatal rat cortical neurons on MEA plates. Exposure to organoid proteins and control is followed by recording of neuronal activity and cell viability assessment.

(B–D) Quantification of neuronal activity measured as 'mean spike rate' (B), 'mean burst rate' (C) and 'mean network burst rate' (D) normalized to culture well-matched vehicle control. Exposure to venom gland organoid supernatant and recombinant alpha bungarotoxin. Paired t test: ****p < 0.0001, ***p = 0.0002, **p = 0.005. Data points represent biological replicates.

(E–G) Cell viability assessment using CFDA, Neutral red and Alamar blue. Normalized to vehicle control (100%). Differences are not significant (n.s.). Data points represent biological replicates.